JGR Oceans

RESEARCH ARTICLE
10.1029/2020JC016859

Submarine Groundwater Discharge on the Western Shelf of the Northern South China Sea Influenced by the Pearl River Plume and Upwelling

Guiyuan Dai[1], Guizhi Wang[1,2], Qing Li[1], Ehui Tan[3], and Minhan Dai[1]

[1]State Key Laboratory of Marine Environmental Science and College of Ocean and Earth Sciences, Xiamen University, Xiamen, China, [2]Fujian Provincial Key Laboratory for Coastal Ecology and Environmental Studies, Xiamen University, Xiamen, China, [3]State Key Laboratory of Marine Resource Utilization in South China Sea, Hainan University, Haikou, China

Key Points:

- Submarine groundwater discharge on the plume-and-upwelling-influenced western shelf of the northern South China Sea was estimated
- Submarine groundwater discharge was a nutrient and carbon source more important than the upwelling and second to the Pearl River
- Submarine groundwater discharge can support 11%–13% of the new production on the shelf

Supporting Information:

Supporting Information may be found in the online version of this article.

Correspondence to:

G. Wang,
gzhwang@xmu.edu.cn

Citation:

Dai, G., Wang, G., Li, Q., Tan, E., & Dai, M. (2021). Submarine groundwater discharge on the western shelf of the northern South China Sea influenced by the Pearl River plume and upwelling. *Journal of Geophysical Research: Oceans*, *126*, e2020JC016859. https://doi.org/10.1029/2020JC016859

Received 6 OCT 2020
Accepted 10 MAR 2021

Abstract Submarine groundwater discharge (SGD) is a crucial material transport pathway across the continent–ocean margins. To evaluate the geochemical impacts of SGD on the western shelf of the northern South China Sea (NSCS), salinity, temperature, and radium were investigated in the summer of 2012. With Ra box models, the flux of SGD was estimated to be $(1.0 \pm 0.44) \times 10^8$ m^3 day^{-1} (3.0 ± 1.3 cm day^{-1}) in the upwelling-influenced area and $(5.4 \pm 2.3) \times 10^8$ m^3 day^{-1} (1.8 ± 0.8 cm day^{-1}) in the no-upwelling area. The flux of SGD in the no-upwelling area estimated using a three end-member mixing model was $(2.1 \pm 1.7) \times 10^8$ m^3 day^{-1} (0.7 ± 0.5 cm day^{-1}), consistent with the flux estimates above. In the upwelling-influenced area, the average net fluxes of dissolved inorganic nitrogen (DIN), soluble reactive phosphorus (SRP), dissolved silicate (DSi), dissolved carbon (including dissolved inorganic carbon, DIC, and organic carbon), and total alkalinity (TA) via SGD were 1–27 times greater than those from the upwelling. In the no-upwelling area, the average SGD-associated DIN, SRP, DSi, TA, and dissolved carbon fluxes were 22%–42% equivalent to the Pearl River estuarine exports. The net SRP flux from SGD could support 11%–13% of the new production on the shelf. The concentration of DIC on the shelf could increase by about 50 μmol L^{-1} due to the net DIC fluxes via SGD. These results indicate that SGD is a significant nutrient and carbon source more important than the upwelling and second to the Pearl River on the western shelf of the NSCS and needs to be considered in the shelf biogeochemistry.

Plain Language Summary The coastal groundwater has been increasingly recognized as a significant nutrient and carbon source to coastal oceans. In this study, we estimated the fluxes of nutrients and carbon via submarine groundwater into the western shelf of the northern South China Sea in the summer of 2012 when both river plumes and upwelling cooccurred on the shelf. We found that submarine groundwater was a vital nutrient and carbon source with material fluxes one fifth to half as much as those exported from the Pearl River in the no-upwelling area, while 1–27 times greater than the inputs from the coastal upwelling in the upwelling-influenced area. With a high N:P ratio of 69, submarine groundwater might significantly promote the primary production in areas limited by nitrogen on the shelf. The carbon and nutrients from submarine groundwater discharge can support 11%–13% of the new production on the western shelf of the northern South China Sea.

1. Introduction

Submarine groundwater discharge (SGD) is defined as the flow of water across the continent–ocean margins from the seabed to the coastal ocean, regardless of fluid composition or driving force (Burnett et al., 2003). SGD is a significant transport pathway for terrestrial materials, including carbon, nutrients, and metals, to enter the coastal ocean (Charette et al., 2013; J. Liu et al., 2017; Q. Liu et al., 2014; Moore et al., 2006; Trezzi et al., 2016; X. Wang et al., 2018). SGD is usually characterized by high nitrogen:phosphorus ratio relative to the Redfield ratio (N:P = 16) (Redfield et al., 1963) and low pH and dissolved oxygen (DO) relative to the values in typical surface seawater. Thus, SGD has been demonstrated to have a significant impact on coastal eutrophication, acidification, and hypoxia (Hwang et al., 2005; McCoy et al., 2011; Santos et al., 2011, 2012; G. Wang et al., 2014). According to Q. Liu et al. (2018), the SGD-derived nutrients fluxes may play a vital role in controlling the nutrient budgets and stoichiometry, in comparison with the nutrient fluxes from rivers,

and the abundant dissolved inorganic nitrogen (DIN) and soluble reactive phosphorus (SRP) fluxes via SGD with a high DIN:SRP ratio into the Pearl River estuary would potentially contribute to eutrophication and red tides in the adjacent waters. G. Wang et al. (2014) found that the low pH water of SGD was a significant contributor to coastal acidification, posing an additional stress on coastal coral reef systems. McCoy et al. (2011) suggested that the Long Bay water slowly collected nutrients and organic carbon from SGD and high rates of heterotrophic activity were thus driven by warm temperature in shallow nearshore waters to draw down DO in the bottom water.

There are three spatial scales of SGD, the nearshore scale, the embayment scale, and the shelf scale, with scale lengths of meters to kilometers (Bratton, 2010; Moore, 2010). So far, SGD studies have been carried out mostly in estuaries, bays, and harbors in terms of nutrient fluxes and their biogeochemical impacts on local aquatic systems (Charette et al., 2013; Gómez-Álvarez et al., 2019; Srinivasamoorthy et al., 2018). Few SGD studies, however, have been focused on the shelf scale regarding the impacts on carbon cycle and primary production (Kim et al., 2011; Q. Liu et al., 2012, 2014; Sadat-Noori et al., 2015).

Radium isotopes are useful naturally occurring radioisotope tracers of SGD, because the activity of Ra is often much higher in saline groundwater than in river water and seawater and Ra is not reactive after being released into seawater, which means that a small SGD input would cause a strong signal in receiving waters (Moore, 2010). There are four radium isotopes, two short-lived radium isotopes, ^{223}Ra (half-life = 11 days) and ^{224}Ra (half-life = 3.66 days), and two long-lived radium isotopes, ^{226}Ra (half-life = 1,600 years) and ^{228}Ra (half-life = 5.75 years). Therefore, radium isotopes are widely used, often with dual isotopes, to estimate process rates in different time scales, for example, a residence time, mixing rates, and the flux of SGD (Charette et al., 2013; Krest et al., 1999; Moore & de Oliveira, 2008; G. Wang et al., 2018).

The northern South China Sea (NSCS) shelf is a unique system affected by both coastal upwellings and the Pearl River plume in summer (Cao et al., 2011). Among the summertime coastal upwellings, the one off the east coast of Hainan Island is an important upwelling center on the western shelf off the Pearl River estuary (Jing et al., 2009; M. Li et al., 2018; P. Lin, Cheng, et al., 2016; P. Lin, Hu, et al., 2016), which was first noticed by Niino and Emery (1961). Most summertime SGD studies in the NSCS were focused on rivers, lagoons, and the eastern shelf off the Pearl River estuary (Ji et al., 2013; Su, Du, Moore, et al., 2011; X. Wang & Du, 2016) with a couple touching on the upwelling areas along the eastern coast of Hainan Island and on the eastern shelf off the Pearl River estuary (Q. Liu et al., 2012; Luo et al., 2018). To our knowledge, no SGD study has ever been carried out on the western shelf off the Pearl River estuary in a summer when the Pearl River plume spreads predominantly in this region.

The objectives of this study were to estimate the flux of SGD on the western NSCS shelf off the Pearl River estuary and to evaluate the geochemical impact of SGD relative to the influences of the coastal upwelling and the Pearl River plume on the shelf biogeochemistry. To achieve these objectives, long-lived radium isotopes were utilized as SGD tracers. In addition, the carbon and nutrient fluxes carried by SGD were quantified and their effects on the shelf carbon budget and their contributions to the new production were discussed.

2. Materials and Methods

2.1. Study Area

The South China Sea, a semienclosed marginal sea in the western Pacific, is influenced by the East Asian monsoon, which is northeasterly in winter and southwesterly in summer (Q. Liu et al., 2018). The Pearl River, with an average discharge of 3.26×10^{11} m^3 year^{-1}, is the third largest river in China, with about 80% of the discharge taking place from April to October (Guo et al., 2008), generating a strong river plume on the shelf of the NSCS. Four types of major plumes may appear in summer, offshore bulge spreading, west alongshore spreading, east offshore spreading, and symmetrical alongshore spreading, depending on river mouth conditions, winds, and ambient coastal currents (Ou et al., 2009).

Hainan Island, the second largest island in China, is located in the northwestern South China Sea. The east coast of Hainan Island is affected by local rivers, SGD, and summer upwelling (Dong et al., 2017; P. Lin, Cheng, et al., 2016; Luo et al., 2018; Su, Du, Moore, et al., 2011). The summer upwelling off the east coast of

Hainan Island is generally driven by the southwest monsoon (P. Lin, Hu, et al., 2016). Wanquan River and Wenjiao and Wencang Rivers are the major fresh water sources to the east coast of Hainan Island. The total water discharge of the two rivers is approximately 6×10^9 m^3 $year^{-1}$, about 2% equivalent to the Pearl River discharge (Dong et al., 2017).

2.2. Sampling and Measurements

Our cruise was conducted from July 28 to August 21, 2012 onboard R/V Dongfanghong II on the shelf of the NSCS. On the western shelf off the Pearl River estuary, water samples were collected along nine transects, from left to right, Transects A–H and K, at 31 stations, from nearshore to offshore, Stations A1, A2, ..., K4, with profiles investigated at 10 stations (Figure 1). On the eastern shelf off the Pearl River estuary, surface seawater samples were collected at four stations from the Pearl River estuary to the east of Taiwan shoals to get a better picture of the Pearl River plume spreading. In addition, Station TS was sampled in the summer of 2009 and taken as the offshore seawater end-member. On the shelf, the riverine contribution is actually what is exported from the estuary. Station F414, located at the mouth of the Pearl River estuary and investigated on July 27, 2012, was therefore taken as the Pearl River end-member. Coastal groundwater samples were collected at eight sites from Zhuhai City to Zhanjiang City from April 6 to 12, 2012.

Surface seawater samples (about 100 L) for radium were collected into a plastic container using a plastic bucket. The temperature and salinity of these samples were measured using a multisensor detector WTW 340i. Intermediate and bottom water samples (22–45 L) were collected using Niskin bottles mounted on a rosette sampler equipped with a calibrated Seabird SBE 911 or 917 conductivity–temperature–depth (CTD) recorder. Afterward, the water samples were pumped through a 1-μm polypropylene cartridge to remove particles before flowing through 16 g MnO_2-impregnated acrylic fiber (Mn-fiber) at a flow rate less than 1 L min^{-1} to accumulate radium (Moore, 1976). Samples for nutrients, dissolved inorganic carbon (DIC), total alkalinity (TA), and dissolved organic carbon (DOC) were collected using Niskin bottles. The sampling and measurement of TA and DIC were detailed in Guo et al. (2008). The precision of DIC and TA measurements is ±2 μmol kg^{-1} (Guo et al., 2008). The sampling and measurement procedures of DOC and nutrients, including DIN, SRP, and dissolved silicate (DSi), were shown in Callahan et al. (2004) and Han et al. (2012), respectively. DIN is the sum of nitrate (NO_3^-), nitrite (NO_2^-), and ammonium (NH_4^+). The precision of DOC measurements is 2%. The quantification limit is 0.1 μmol L^{-1} for $NO_2^- + NO_3^-$, 0.08 μmol L^{-1} for DIP, 0.16 μmol L^{-1} for DSi (Han et al., 2012), and 0.5 μmol L^{-1} for NH_4^+.

Coastal groundwater samples were collected on sandy beaches using a Pushpoint sampler and a peristatic pump. Ra samples were about 8 L. The samples for nutrients, DIC, TA, and DOC were collected and measured with the same method as for the seawater.

2.3. Measurements of Ra Isotopes

In the laboratory, sea salts on the Mn-fibers were removed with Ra-free deionized water. Then moisture was adjusted to approximately 1:1 fiber:water ratio (Moore, 2007; Yin & Torgersen, 1998) before placing the Mn-fibers into the circulation system of a Radium Delayed Coincidence Counter (RaDeCC) to measure for ^{223}Ra and ^{224}Ra (Moore, 2003, 2007; Moore & Arnold, 1996). After measurements of ^{223}Ra and ^{224}Ra, the Mn-fibers were leached with a mixture of 1 M hydroxylamine hydrochloride and 1 M HCl at a ratio of 2:1 at 80°C–90°C to remove radium, which was then coprecipitated with $BaSO_4$ and measured for ^{226}Ra and ^{228}Ra using a Canberra germanium well-type gamma detector (Elsinger et al., 1982; Michel et al., 1981; Moore & Dymond, 1984; Tan et al., 2018; X. Wang & Du, 2016). Considering the error propagation from counting statistics, counter calibration, chance coincidence corrections, and variations in sample extraction, the measurement error for ^{223}Ra falls within 60%. The measurement error for ^{224}Ra falls within 40%. The error for long-lived radium measurements is no more than 9%.

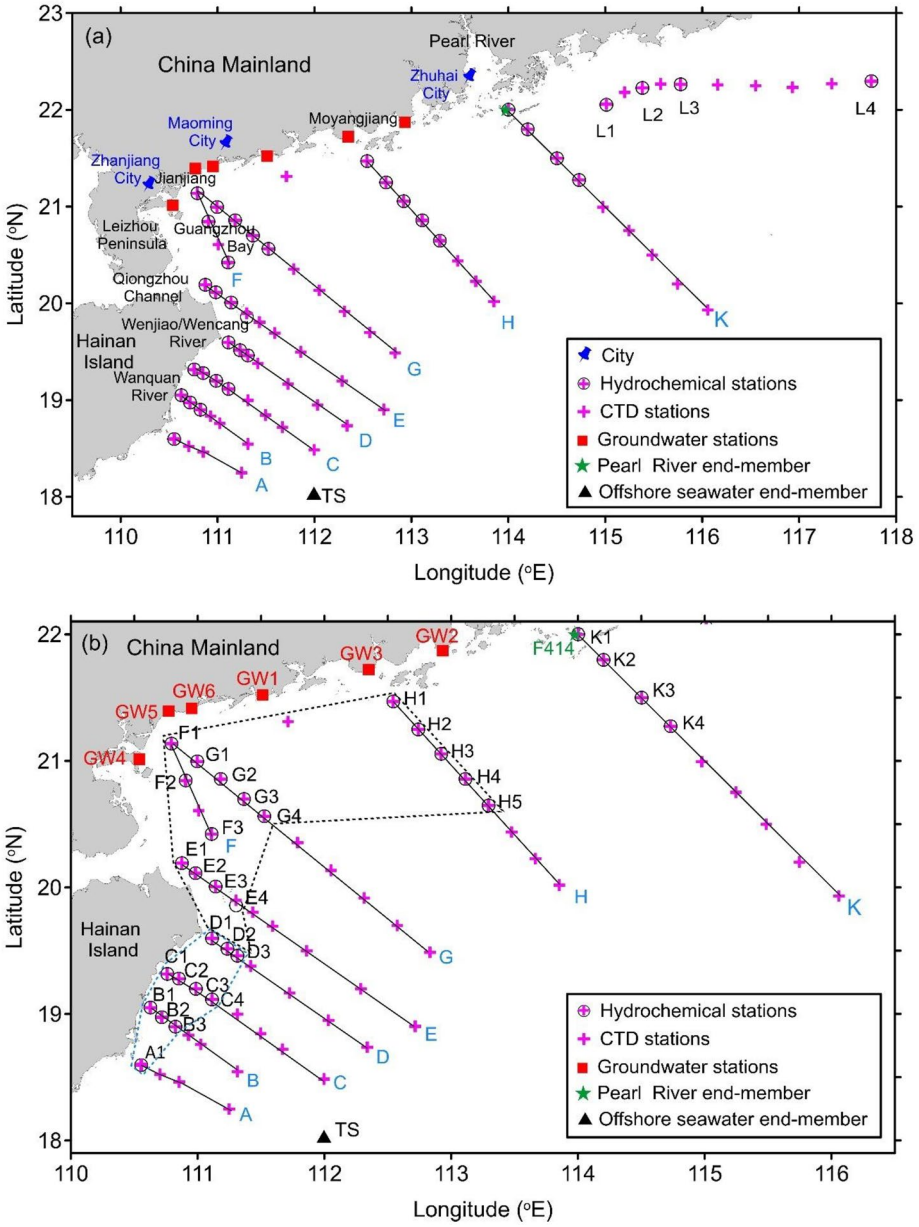

Figure 1. Sampling sites on the northern South China Sea shelf. (a) Geographical names and stations in the study area, and (b) stations on the western shelf off the Pearl River estuary. There are nine cross-shelf transects, A–H and K from left to right on the western shelf. The upwelling-influenced area (the blue dashed box) and the no-upwelling area (the black dashed box) are connected via Transect D.

2.4. Calculations

2.4.1. The Residence Time Based on $ex^{223}Ra/ex^{228}Ra$ Activity Ratio

Residence time is defined as the time required for a particle or a water parcel to reach the outlet (Eleftheriou et al., 2017; Takeoka, 1984; Zimmerman, 1976). It has been widely used to describe the temporal scale of water mixing and transport (Eleftheriou et al., 2017; Lee et al., 2014; Men et al., 2016; Nozaki et al., 1989; Tan et al., 2018). The residence time on the western shelf off the Pearl River estuary was estimated to be 18 ± 8 days in winter (Tan et al., 2018). We expected that the residence time was in the same order of magnitude in summer in this area. Most of ^{224}Ra would have decayed within this residence time on the western shelf. The differences in the activity of ^{226}Ra among different water sources are much smaller than those

in ^{228}Ra so that changes in the isotopic ratio are much less significant for ^{226}Ra than for ^{228}Ra on the shelf. So, we chose to use the isotopic ratio ^{223}Ra/^{228}Ra to calculate the residence time in this study. According to Moore (2000), in areas where an apparent Ra point source is persistent and there is no additional source of Ra after the water leaves the Ra source, the residence time can be approximated with an apparent water age model using the following equation:

$$\left[\frac{ex^{223}Ra}{ex^{228}Ra}\right]_{obs} = \left[\frac{ex^{223}Ra}{ex^{228}Ra}\right]_{i} e^{-\lambda_{223}t} \quad (1)$$

where λ_{223} is the decay constant of ^{223}Ra (0.0608 day^{-1}), t is the residence time (days), ex represents the excess radium, which is the activity of radium subtracting the radium activity of the offshore surface water (0 for ^{223}Ra and 8.24 dpm 100 L^{-1} for ^{228}Ra, the activities at Station TS), $\left[\frac{ex^{223}Ra}{ex^{228}Ra}\right]_{obs}$ is the excess activity ratio in the study area, and $\left[\frac{ex^{223}Ra}{ex^{228}Ra}\right]_{i}$ denotes the excess activity ratio of the radium source.

In areas with continuous radium additions such as from upwelling and SGD, Equation 1 is inappropriate to calculate the residence time. The residence time can be estimated using the following equation posed by Moore et al. (2006):

$$t = \left[F\left(\frac{ex^{223}Ra}{ex^{228}Ra}\right) - I\left(\frac{ex^{223}Ra}{ex^{228}Ra}\right)\right] / I\left(\frac{ex^{223}Ra}{ex^{228}Ra}\right)\lambda_{223} \quad (2)$$

where $F\left(\frac{ex^{223}Ra}{ex^{228}Ra}\right)$ is the flux ratio of the main radium source, which equals the radium activity ratio of the main radium source in the study area, and $I\left(\frac{ex^{223}Ra}{ex^{228}Ra}\right)$ is the radium inventory ratio, which equals the observed radium activity ratio in the study area.

2.4.2. Box Model

Under the assumption of steady state, the radium additions from rivers, sediment diffusion, upwelling, and SGD are balanced by radium losses, including decay and mixing with the offshore seawater. The flux of SGD can then be estimated based on the mass balance of radium in the box under consideration (Q. Liu et al., 2014; Moore, 1996; Moore et al., 2008; Tan et al., 2018). On the western shelf off the Pearl River estuary, the mass balance of radium is described below (Figure S1):

$$\frac{{}^{i}I}{t} = \Sigma\left(Q_{riv} \times {}^{i}Ra_{riv}\right) + A_{sed} \times {}^{i}F_{sed} + Q_{SGD} \times {}^{i}Ra_{SGD} + v \times {}^{i}Ra_{uw} \times A_{uw} + \Sigma\left(Q_{ht} \times {}^{i}Ra_{ht}\right) \quad (3)$$

where ${}^{i}I$ (dpm) is the excess radium inventory in the mixed layer in the study area and the superscript i represents 226 or 228, Q_{riv} (m^3 day^{-1}) is the river discharge, ${}^{i}Ra_{riv}$ (dpm 100 L^{-1}) is the activity of ${}^{i}Ra$ of the river end-member, A_{sed} (m^2) is the sediment area, ${}^{i}F_{sed}$ (dpm m^{-2} day^{-1}) is the diffusion flux of ${}^{i}Ra$ from sediments, $Q_{SGD} \times {}^{i}Ra_{SGD}$ represents the flux of ${}^{i}Ra$ from SGD, where Q_{SGD} (m^3 day^{-1}) and ${}^{i}Ra_{SGD}$ are the flux of SGD and the activity of ${}^{i}Ra$ in the groundwater end-member, respectively, $v \times {}^{i}Ra_{uw} \times A_{uw}$ is the flux of ${}^{i}Ra$ delivered by the upwelling, where v (m day^{-1}), ${}^{i}Ra_{uw}$ (dpm 100 L^{-1}), and A_{uw} (m^2) denote the upwelling rate, the activity of ${}^{i}Ra$ in the subsurface water, and the area of upwelling, respectively, and $\Sigma(Q_{ht} \times {}^{i}Ra_{ht})$ represents the total horizontal transport flux across all the boundaries of the box, including alongshore transport and offshore transport, where Q_{ht} is the net transport flux at each boundary of the box and ${}^{i}Ra_{ht}$ is the average radium activity at each boundary of the box. Q_{ht} is from the model data based on the Regional Ocean Model System and level-2.5 turbulent kinetic energy equation for three-dimensional, time-dependent oceanographic flows, and vertical mixing parameterization, respectively (Gan et al., 2009, 2010).

The activity of radium in the mixed layer can be represented by the radium activity in the surface seawater. To estimate ${}^{i}I$, three adjacent stations were connected to form a triangle. Assume the number of triangles in

the box is n. The radium inventory of the jth triangle ($j = 1, 2, ..., n$) is the product of the surface area of the triangle, A_j (m^2), the average excess radium activity, ex^iRa_j (dpm 100 L^{-1}), and the average mixed layer depth, H_j (m), of the three stations in the triangle. The sum of the excess radium inventories of all the triangles is ^iI, that is,

$$^iI = \sum_{j=1}^{n}\left(A_j \times H_j \times ex^iRa_j\right) \tag{4}$$

2.4.3. Three End-Member Mixing Model

Mixing models can be applied to estimate the fraction of each end-member considering the conservation of specific parameters (Moore, 2003; G. Wang et al., 2018). In this study, a three end-member mixing model can be established considering the conservation of water and long-lived radium isotopes as follows:

$$\begin{cases} f_{sw} + f_{GW} + f_{riv} = 1 \\ {}^{226}Ra_{sw}f_{sw} + {}^{226}Ra_{GW}f_{GW} + {}^{226}Ra_{riv}f_{riv} = {}^{226}Ra_{obs} \\ {}^{228}Ra_{sw}f_{sw} + {}^{228}Ra_{GW}f_{GW} + {}^{228}Ra_{riv}f_{riv} = {}^{228}Ra_{obs} \end{cases} \tag{5}$$

where the subscripts sw and GW represent the offshore seawater end-member and groundwater end-member, respectively, riv refers to the Pearl River end-member, obs represents the observed data, and f is the fraction of each end-member. Thus, f can be solved as

$$\begin{cases} f_{sw} = \dfrac{\dfrac{{}^{226}Ra_{obs} - {}^{226}Ra_{riv}}{{}^{226}Ra_{GW} - {}^{226}Ra_{riv}} - \dfrac{{}^{228}Ra_{obs} - {}^{228}Ra_{riv}}{{}^{228}Ra_{GW} - {}^{228}Ra_{riv}}}{\dfrac{{}^{226}Ra_{sw} - {}^{226}Ra_{riv}}{{}^{226}Ra_{GW} - {}^{226}Ra_{riv}} - \dfrac{{}^{228}Ra_{sw} - {}^{228}Ra_{riv}}{{}^{228}Ra_{GW} - {}^{228}Ra_{riv}}} \\ f_{riv} = \dfrac{\dfrac{{}^{226}Ra_{obs} - {}^{226}Ra_{sw}}{{}^{226}Ra_{GW} - {}^{226}Ra_{sw}} - \dfrac{{}^{228}Ra_{obs} - {}^{228}Ra_{sw}}{{}^{228}Ra_{GW} - {}^{228}Ra_{sw}}}{\dfrac{{}^{226}Ra_{riv} - {}^{226}Ra_{sw}}{{}^{226}Ra_{GW} - {}^{226}Ra_{sw}} - \dfrac{{}^{228}Ra_{riv} - {}^{228}Ra_{sw}}{{}^{228}Ra_{GW} - {}^{228}Ra_{sw}}} \\ f_{GW} = \dfrac{\dfrac{{}^{226}Ra_{obs} - {}^{226}Ra_{sw}}{{}^{226}Ra_{riv} - {}^{226}Ra_{sw}} - \dfrac{{}^{228}Ra_{obs} - {}^{228}Ra_{sw}}{{}^{228}Ra_{riv} - {}^{228}Ra_{sw}}}{\dfrac{{}^{226}Ra_{GW} - {}^{226}Ra_{sw}}{{}^{226}Ra_{riv} - {}^{226}Ra_{sw}} - \dfrac{{}^{228}Ra_{GW} - {}^{228}Ra_{sw}}{{}^{228}Ra_{riv} - {}^{228}Ra_{sw}}} \end{cases} \tag{6}$$

Then, the flux of SGD (m^3 day^{-1}) can be estimated:

$$Q_{SGD} = f_{GW} \times V_{sw} / t \tag{7}$$

where V_{sw} (m^3) is the volume above the mixed layer of the study area, which can be determined using the same triangle approach as that in calculating ^iI.

2.4.4. Error Estimation

The uncertainty in a function, $F = f(x_1, x_2, ..., x_n)$, resulting from the errors in $x_1, x_2, ..., x_n$ can be derived as follows (Taylor, 1997; G. Wang et al., 2015):

$$\delta F = \sqrt{\sum_{i=1}^{n}\left(\frac{\partial F}{\partial x_i}\delta_{x_i}\right)^2} \tag{8}$$

where δF and δx_i are the uncertainty in F and x_i ($i = 1, 2, ..., n$), respectively. The uncertainties in the residence time and flux estimations were thus calculated following Equation 8. The details of the uncertainty estimation were shown in the Supporting Information.

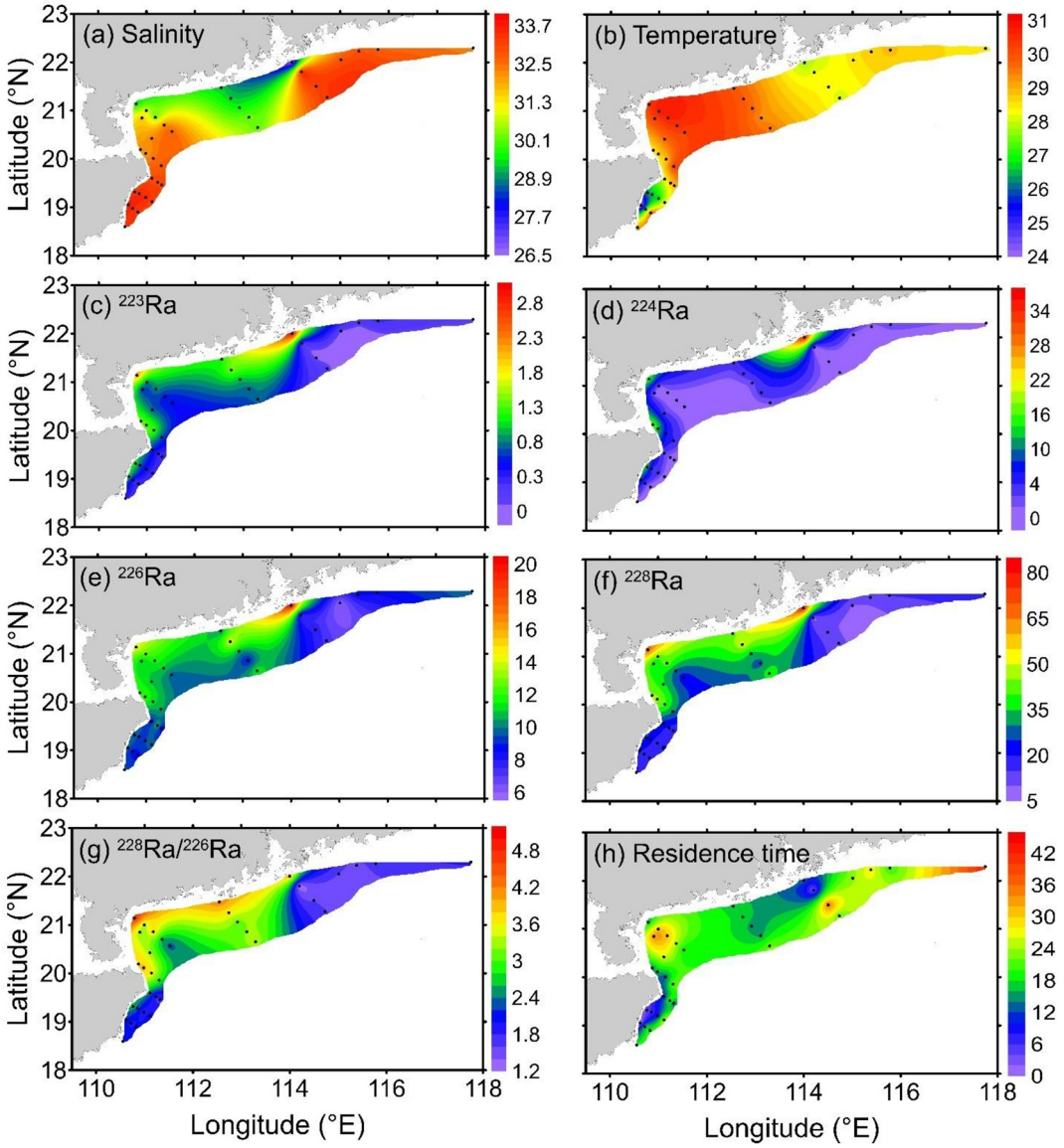

Figure 2. Surface distributions of (a) salinity, (b) temperature (°C), (c) ^{223}Ra (dpm 100 L^{-1}), (d) ^{224}Ra (dpm 100 L^{-1}, corrected for the ingrowth from ^{228}Th), (e) ^{226}Ra (dpm 100 L^{-1}), (f) ^{228}Ra (dpm 100 L^{-1}), (g) ^{228}Ra/^{226}Ra, and (h) residence time (day) on the shelf of the northern South China Sea during the cruise from July 28 to August 21, 2012.

3. Results

3.1. Hydrographic Characteristics

The distributions of surface seawater temperature and salinity were shown in Figure 2, which were consistent with the data at 5 m below the sea surface presented in P. Lin, Hu, et al. (2016). The surface salinity ranged from 26.7 to 33.9 (Figure 2a). The lowest salinity appeared at Station K1 near the Pearl River estuary, and the salinity gradually increased westward and southwestward from the Pearl River estuary to the Qiongzhou Channel, suggesting the westward spreading of the Pearl River plume. In the nearshore region along the coast between Zhanjiang City and Maoming City, there was a local salinity minimum with salinity <30. From Guangzhou Bay to the east coast of Hainan Island, the salinity increased from 29.6 to 33.9. The local maximum salinity of 33.9 (at Station B1) off the east coast of Hainan Island coincided with the local minimum surface seawater temperature of 24.0°C (Figures 2a and 2b). The relatively low seawater temper-

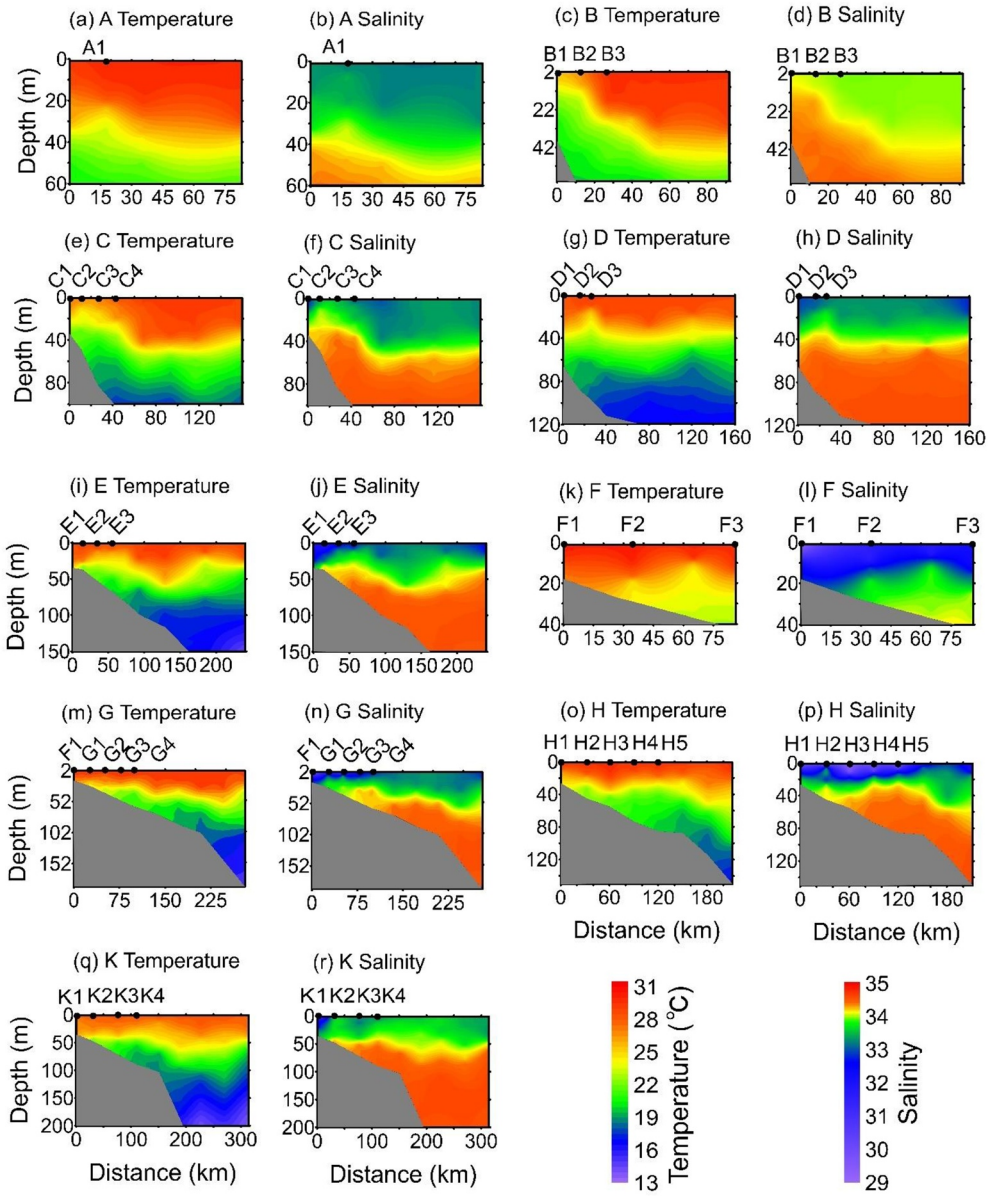

Figure 3. Vertical distributions of seawater temperature (°C) and salinity along nine transects on the western shelf of the northern South China Sea during the period from July 28 to August 21, 2012. The radiolabeled stations are hydrochemical stations. (a and b) Transect A, (c and d) Transect B, (e and f) Transect C, (g and h) Transect D, (i and j) Transect E, (k and l) Transect F, (m and n) Transect G, (o and p) Transect H, and (q and r) Transect K.

ature and relatively high salinity along the east coast of Hainan Island indicate the occurrence of coastal upwelling in this area.

The surface seawater temperature ranged from 24.0°C to 30.7°C (Figure 2b). Near the Pearl River estuary, the temperature was relatively low (at Station K1). Away from the Pearl River estuary, the surface temperature increased westward until reaching the Qiongzhou Channel. From Guangzhou Bay southward to the east coast of Hainan Island, however, the temperature decreased from 30.7°C to 24.0°C under the influence of the coastal upwelling off the east coast of Hainan Island.

As shown by the vertical distributions of seawater temperature and salinity (Figure 3), a water mass with relatively low temperature and high salinity was observed to climb shoreward along Transect A from 30 m below the sea surface (Figures 3a and 3b), indicating that upwelling was occurring in the subsurface in this

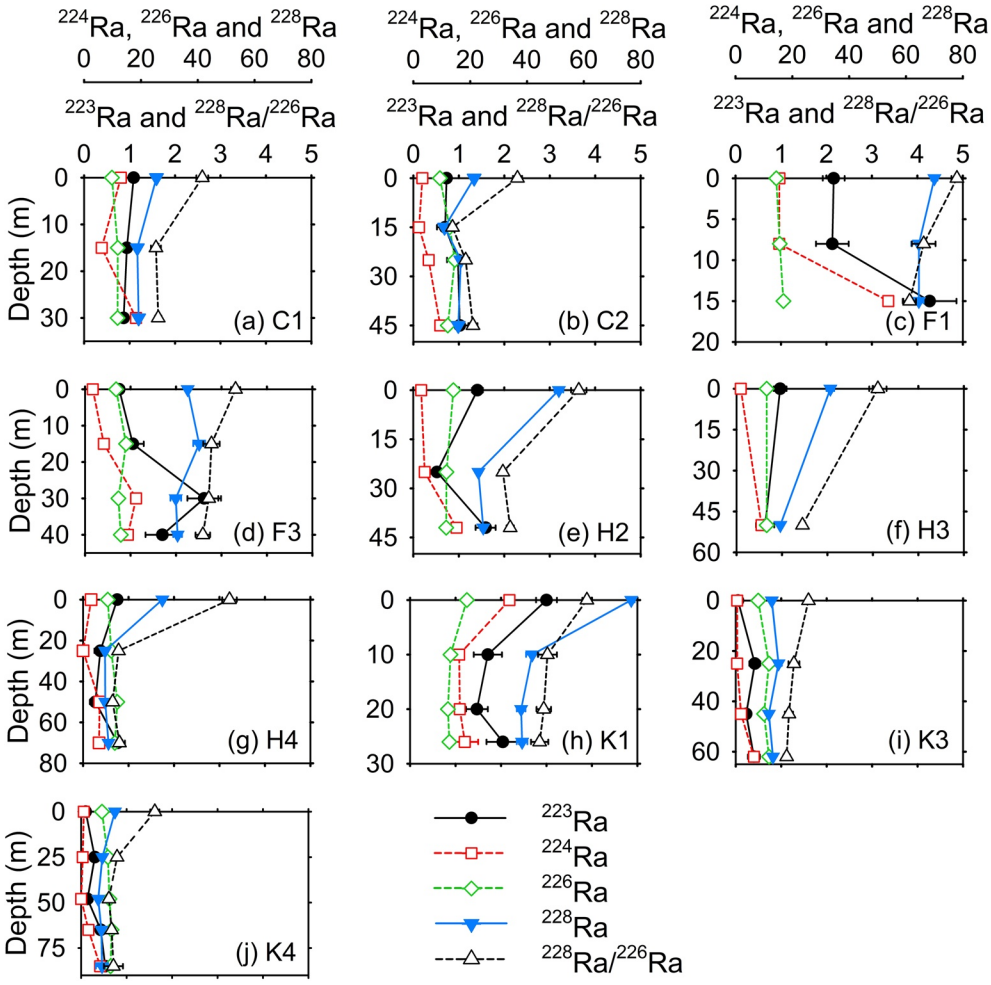

Figure 4. Vertical distributions of $^{223,224,226.228}$Ra activities (dpm 100 L^{-1}) and ^{228}Ra/^{226}Ra ratios on the western shelf of the northern South China Sea from July 28 to August 21, 2012. (a) Station C1, (b) Station C2, (c) Station F1, (d) Station F3, (e) Station H2, (f) Station H3, (g) Station H4, (h) Station K1, (i) Station K3, and (j) Station K4.

area. Waters with relatively low temperature and high salinity were also observed to climb upward along the slope off the east coast of Hainan Island and outcrop nearshore at Station B1 (Figures 3c–3f). Relatively low salinity (<33.0) was observed nearshore at water depth shallower than 10 m along Transect C, which was caused by the Wanquan River and Wenjiao and Wencang Rivers. Along Transect D, the upwelling was not obvious and the water was well stratified (Figures 3g and 3h). A remarkably low salinity (<32.8) was observed in the nearshore water at water depth above 27 m along Transect E (Figure 3j). In addition, relatively low salinity (<32.6) was observed in the whole water column nearshore and the salinity increased offshore along Transects F and G in Guangzhou Bay (Figures 3l and 3n), indicating the influence of local rivers. An upwelling was observed with a center between Stations F2 and F3 at water depth deeper than 10 m. A water mass with relatively low temperature and high salinity was observed along Transect G at water depth deeper than 20 m (Figures 3m and 3n), indicating the occurrence of upwelling in the subsurface in this area and that the local river plumes obviously blocked its outcropping. Along Transects H and K, relatively low salinity (<33.3) was observed in the surface layer (Figures 3p and 3r), which was caused by the Pearl River plume. Upwelling of relatively low temperature and high salinity water was observed at water depth deeper than 40 m along Transect H (Figures 3o and 3p). These observations demonstrate that the coastal upwelling off the east coast of Hainan Island occurred along Transects A–C and outcropped at Station B1, upwelling occurred in the subsurface at water depth deeper than 10, 20, and 40 m along Transects F–H, respectively, while the river plumes affected Transects C–H and K. In the no-upwelling area, the water is stratified with an average mixed layer depth of 8.8 m (Figure S2).

Table 1
Definitions and Values of Parameters Used in the Box Model of ^{226}Ra and ^{228}Ra to Calculate Submarine Groundwater Discharge on the Western Shelf of the Northern South China Sea

	Definition	^{226}Ra	^{228}Ra	Unit
Ra_{SGD}	Radium activity of the groundwater end-member	86 ± 52	751 ± 643	dpm 100 L^{-1}
Ra_{sw}	Radium activity of the offshore seawater end-member	4.9 ± 0.1	8.2 ± 0.3	dpm 100 L^{-1}
Ra_{uw}	Radium activity of the upwelling end-member	11.8 ± 0.5	18.7 ± 1.1	dpm 100 L^{-1}
Ra_{quan}	Radium activity of the Wanquan River end-member[b]	12.8 ± 0.4	31 ± 1	dpm 100 L^{-1}
Ra_{wen}	Radium activity of the Wenjiao and Wencang Rivers end-member[b]	24 ± 1	126 ± 4	dpm 100 L^{-1}
Ra_{PR}	Radium activity of the Pearl River end-member	25 ± 1	86 ± 3	dpm 100 L^{-1}
Ra_{jian}	Radium activity of the Jianjiang River	36 ± 1	91 ± 3	dpm 100 L^{-1}
Ra_{my}	Radium activity of the Moyangjiang River	17.7 ± 0.4	80 ± 2	dpm 100 L^{-1}
$^{i}F_{sed}$	Sediment diffusion flux of Ra	0.45[a]	6.3[b]	dpm m^{-2} d^{-1}
Q_{quan}	Discharge of the Wanquan River[c]	2.3×10^7	–	m^3 d^{-1}
Q_{wen}	Discharge of the Wenjiao and Wencang Rivers[c]	3.6×10^6	–	m^3 d^{-1}
Q_{jian}	Discharge of the Jianjiang River[d]	2.4×10^7	–	m^3 d^{-1}
Q_{my}	Discharge of the Moyangjiang River	3.4×10^7	–	m^3 d^{-1}
A_{uw}	Surface area of the upwelling zone	3.4×10^9	–	m^2
A_{sed1}	Surface area of the sediment in the upwelling-influenced area	3.4×10^9	–	m^2
A_{sed2}	Surface area of the sediment in the no-upwelling area	3.0×10^{10}	–	m^2

[a]Q. Liu et al. (2012). [b]Luo et al. (2018). [c]Su, Du, Ji, et al. (2011). [d]Q. Li (2014).

3.2. Distributions of Radium Isotopes

The activities (in dpm 100 L^{-1}) of ^{223}Ra, ^{224}Ra, ^{226}Ra, and ^{228}Ra ranged from 0.05 ± 0.02 to 2.16 ± 0.24, from 0 to 35.0 ± 1.2, from 5.92 ± 0.17 to 20.0 ± 0.4, and from 9.50 ± 0.45 to 78 ± 1, respectively (Figures 2c–2f). The maximal radium activity appeared near the Pearl River estuary at Station K1 and decreased along the spreading path of the Pearl River plume because of decay and mixing with ambient seawaters. Due to the short half-lives of ^{223}Ra and ^{224}Ra, the activities of ^{223}Ra and ^{224}Ra decreased offshore much faster, while ^{226}Ra and ^{228}Ra with relatively high activities spread all over the western shelf off the Pearl River estuary. At Station F1, the most nearshore station in Guangzhou Bay, the activities of ^{223}Ra, ^{224}Ra, ^{226}Ra, and ^{228}Ra were 2.16, 15.5, 14.4, and 70.0 dpm 100 L^{-1}, respectively, which were higher than those in adjacent stations. The activities of the long-lived radium seemed to decrease southward from Station F1 along Leizhou Peninsula to the eastern coast of Hainan Island.

The vertical distributions of radium did not follow a consistent pattern (Figure 4). At Stations C1 and C2, the nearshore stations off the east coast of Hainan Island, as shown earlier, the surface water was influenced by local rivers (Wanquan River, and Wenjiao and Wencang Rivers). However, the ^{226}Ra activities in the local rivers were half to a quarter of that in the Pearl River estuary (Table 1), so the ^{226}Ra activities in the surface water were similar to those in the bottom water. In contrast, the activities of ^{228}Ra were relatively high in these coastal rivers, thus, higher activities of ^{228}Ra were observed in the surface water than in the bottom. The $^{228}Ra/^{226}Ra$ ratios in the surface water were higher than those in the subsurface and bottom waters due to the influence of local rivers where the $^{228}Ra/^{226}Ra$ ratios ranged from 2.42 to 5.25 (Figure 3f), much higher than the $^{228}Ra/^{226}Ra$ ratio of the offshore seawater at Station TS, 1.70 ± 0.07. Along Transect F in Guangzhou Bay, the salinity at the nearshore Station F1 was 29.57 in the surface and increased to 32.62 at the depth of 15 m, indicating the influence of coastal rivers in the surface layer. The radium activities at this station are higher than those at stations along Transects C and H and the offshore Stations K3 and K4 throughout the water column. The radium activities in the surface layer, however, were lower than its bottom activities, except for ^{228}Ra, along Transect F. At Station F3, local maxima of the short-lived and long-lived radium appeared at the depth of 30 and 15 m, respectively. Compared with the nearshore Station F1, the activities of radium at offshore Station F3 were less throughout the water column. The $^{228}Ra/^{226}Ra$ ratios ranged from

Table 2
Radium Activities, Nutrients, and Carbon Concentrations of the Coastal Groundwater Along the Coast From Zhuhai City to Zhanjiang City in the Spring of 2012

Station	Latitude (°N)	Longitude (°E)	Sampling depth (m)	Temperature (°C)	Salinity	^{223}Ra	^{224}Ra	^{226}Ra	^{228}Ra	^{228}Ra/^{226}Ra	DIN	SRP	DSi	DIC	TA	DOC	N:P
						dpm 100 L^{-1}					μmol L^{-1}						
GW1	21.5212	111.5120	1.0	22.0	29.3	33 ± 3	552 ± 3	42 ± 2	223 ± 8	5.37	7.2	1.34	48.8	2,236	2,414	57	5.4
GW2-1	21.8706	112.9330	1.4	21.8	23.6	25 ± 3	544 ± 4	73 ± 3	492 ± 15	6.78	9.0	1.24	81.3	2,757	2,910	110	7.2
GW2-2	21.8706	112.9330	1.0	22.2	25.1	20 ± 2	557 ± 2	62 ± 3	369 ± 11	5.95	19.5	0.46	58.4	2,332	–	94	42.2
GW3	21.7224	112.3490	1.0	22.5	24.1	77 ± 7	2,013 ± 6	131 ± 5	1,574 ± 42	12.0	41.3	0.24	50.4	2,160	2,264	70	172
GW4	21.0122	110.5380	1.0	24.8	22.7	7.4 ± 1.7	356 ± 3	31 ± 1	176 ± 6	5.71	49.7	0.72	30.1	2,418	2,562	71	69.0
GW5-1	21.3937	110.7710	2.0	22.1	24.7	82 ± 7	1,730 ± 5	198 ± 5	2,060 ± 40	10.4	267	1.97	179	4,657	4,853	172	135
GW5-2	21.3937	110.7710	1.0	22.8	26.4	55 ± 7	1,217 ± 4	93 ± 2	656 ± 13	7.02	92.4	0.94	93.9	4,408	4,552	132	98.5
GW6	21.4155	110.9520	1.0	24.6	29.5	45 ± 4	831 ± 3	56 ± 2	458 ± 11	8.19	25.0	0.49	58.4	2,217	2,337	70	51.1
Average	na	na	na	22.8	25.7	43	975	86	751	7.68	63.9	0.92	75.1	2,898	3,128	127	na
SD	na	na	na	1.1	2.4	25	576	52	643	2.24	81.1	0.53	43.5	961	1,018	29	na

Abbreviations: na, not applicable; SD, standard deviation.

3.83 to 4.87 at Station F1 and from 2.59 to 3.31 at Station F3. Similar to the vertical pattern at Station F1, the bottom radium activities were greater than the surface at Station F3, except for ^{228}Ra. From the vertical distribution of density (Figure S2), the water deeper than 25 m at Station F3 was well mixed. The ^{228}Ra/^{226}Ra ratios at this station at water depth deeper than 15 m were nearly constant because of the vertical mixing. Q. Liu et al. (2012) presented a similar profile in the upwelling region on the eastern shelf off the Pearl River estuary. Along Transect H with the nearshore Station H1 excluded, the surface layer was apparently dominated by the Pearl River plume. The radium activities in the surface layer were higher than those in the offshore stations. The ^{228}Ra/^{226}Ra ratios in the surface water were greater than 3.11, higher than those in the subsurface and bottom waters. The long-lived ^{228}Ra activity was higher in the surface water or remained almost the same throughout the water column due to the influence of the river plume. However, the activities of ^{223}Ra and ^{224}Ra in the surface water were lower than or equal to those in the bottom due to their relatively short half-lives. The activity of ^{226}Ra at Station H2 was higher in the surface than in the bottom. At further offshore Stations H3 and H4, however, the surface ^{226}Ra activity was lower than the bottom. Along Transect K, the one closest to the Pearl River estuary, the radium activities at nearshore Station K1 were influenced the most by the Pearl River. At further offshore Stations K3 and K4, the radium activities were relatively low, with ^{223}Ra and ^{224}Ra no more than 0.53 and 6.96 dpm 100 L^{-1}, respectively. The activities of ^{226}Ra and ^{228}Ra ranged from 7.32 to 11.7 dpm 100 L^{-1} and 6.02 to 15.0 dpm 100 L^{-1}, respectively. The ^{228}Ra/^{226}Ra ratios were no more than 1.62. The radium activities in the bottom water were a little higher than in the surface, expect for the activity of ^{228}Ra that remains almost the same as that in the surface water.

3.3. Radium, Nutrients, and Carbon in the Coastal Groundwater

The salinity in the coastal groundwater ranged from 22.7 to 29.5, with an average of 25.7 ± 2.4. The temperature ranged from 21.8°C to 24.8°C (Table 2). The radium activity (dpm 100 L^{-1}) in the saline groundwater was generally greater than that in the seawater and showed great spatial variations, 7.4–82 for ^{223}Ra, 356–2013 for ^{224}Ra, 31–198 for ^{226}Ra, and 176–2060 for ^{228}Ra. Nutrients and carbon are also enriched in the saline groundwater. The concentration (μmol L^{-1}) was 63.9 ± 81.1 for DIN, 0.92 ± 0.53 for SRP, 75.1 ± 43.5 for DSi, 2,898 ± 961 for DIC, 3,128 ± 1018 for TA, and 127 ± 29 for DOC. The nitrogen:phosphorus ratios were significantly greater than the Redfield ratio, except GW1 and GW2-1.

4. Discussion

4.1. Residence Time Based on ex^{223}Ra/ex^{228}Ra

As shown in Figure 2a, low salinity (<30) was observed in the nearshore region from Zhanjiang City to Maoming City. P. Lin, Hu, et al. (2016) suggested that the high precipitation over the north of 20°N especially on the Leizhou Peninsula contributed abundant freshwater to local rivers, such as Jianjiang River and Moyangjiang River, and the local rivers then entered the shelf causing a local salinity minimum. Hence, the relatively low salinity in the nearshore region of Zhanjiang City and Maoming City was caused by local river inputs. In addition, relatively high ^{228}Ra/^{226}Ra ratios, 3.00–4.87, were observed in this region (Figure 2g). The surface water in this region was not affected by upwelling or sediments due to stratification as shown in Section 3.1. Among the potential sources of radium to Guangzhou Bay, the ^{228}Ra/^{226}Ra ratio of the local rivers was 2.52 ± 0.02; the average ^{228}Ra/^{226}Ra ratio in the Pearl River estuary was 3.01 ± 0.61 (at stations where salinity >0); the average ratio of the coastal groundwater was 7.68 ± 2.24. Thus,

such high ratios must have resulted from SGD. The decrease in the ratio offshore suggested the offshore decrease in the contribution of SGD. The influence of SGD can be discerned in the whole water column at nearshore Station F1 from the relatively high $^{228}Ra/^{226}Ra$ ratio. However, the $^{228}Ra/^{226}Ra$ ratio was 4.87 in the surface and decreased to 3.83 in the bottom, suggesting that the influence of SGD decreased with water depth at this station. The influence of SGD on the bottom water was inferred to be the greatest at Station F1 than at other stations in this region based on the highest bottom radium activities and $^{228}Ra/^{226}Ra$ ratio. Therefore, combined with the spatial distributions of temperature, salinity, activities of radium, and $^{228}Ra/^{226}Ra$ ratio presented in Section 3, the eastern coast of Hainan Island was influenced by the upwelling and the shelf off the coast from Zhuhai City to Zhanjiang City was affected by the Pearl River, local rivers in Guangzhou Bay, and SGD. In general, the Pearl River plume spreads eastward under the southwestern monsoon in summer (Pang et al., 2006). Yet, in the summer of 2012, the plume flowed westward. The spreading path of the Pearl River plume was affected by the seasonal monsoon wind forcing and sea level variability (Pang et al., 2006). In the summer of 2012, a significant sea level elevation up to 79 mm was observed, caused by a positive anomalous sea surface heat flux and positive freshwater flux (L. Liu et al., 2018). When the southwestern wind was weak, the pressure gradient from west to east was the dominant factor causing the plume to spread westward along the coast of Guangdong Province (Pang et al., 2006).

To determine the residence time on the western shelf, this region was divided into an upwelling-influenced area and a no-upwelling area based on $^{228}Ra/^{226}Ra$ ratios with Transect D as the dividing line (Figure 1b). The $^{228}Ra/^{226}Ra$ ratio ranged from 1.78 to 2.60 in the upwelling-influenced area and from 2.32 to 4.87 in the no-upwelling area.

In the upwelling-influenced area, the upwelling outcropped at nearshore Station B1. Thus, Station B1 was assumed as a surface radium source of the upwelling signal, and its $\frac{ex^{223}Ra}{ex^{228}Ra}$ ratio, 0.083, was used as $\left[\frac{ex^{223}Ra}{ex^{228}Ra}\right]_i$ in Equation 1. The residence time was thus calculated in the upwelling area to be 4.4–24.8 days, with an average of 15.0 ± 6.5 days.

SGD and the Pearl River plume were the predominant sources of radium in the no-upwelling area. As discussed in Section 3.1, Transect H was dominated by the Pearl River plume. We took 0.098 that was the $^{223}Ra/^{228}Ra$ ratio of Station F414 as $\left[\frac{ex^{223}Ra}{ex^{228}Ra}\right]_i$ in Equation 1 in the Pearl River-dominated area. In the SGD-dominated area, the average $^{223}Ra/^{228}Ra$ ratio in the coastal groundwater, 0.070, was used as $F\left[\frac{ex^{223}Ra}{ex^{228}Ra}\right]$ in Equation 2. Therefore, the residence time for the Pearl River-dominated area and SGD-dominated area ranged from 15.2 to 22.1 days with an average of 17.6 ± 2.5 days and 10.6–33.8 days with an average of 21.4 ± 7.4 days, respectively. The average residence time in the no-upwelling area was 20.3 ± 6.6 days. The residence time was generally smaller nearshore, especially near the Pearl River estuary and in the upwelling-influenced area (Figure 2h). In Guangzhou Bay, however, the surface seawater was dominated by SGD and the residence time was greater than in other nearshore areas.

4.2. The Flux of SGD Derived From Ra Box Models

In the Pearl River estuary, the activity of the long-lived radium isotopes decreased linearly with salinity at salinity greater than 9 (Q. Liu et al., 2012), indicating that desorption of radium from total suspended matter (TSM) at salinity greater than 9 was insignificant on the shelf of the NSCS. On the western shelf, the salinity ranged from 26.7 to 33.9. Thus, we can infer that the radium desorbed from TSM contributed little to the radium in this region. In the following discussion, the radium desorbed from TSM was ignored. In the upwelling-influenced area, the long-lived radium isotopes varied with salinity without a consistent pattern (Figures S3a and S3b). Similarly, in the no-upwelling area, there was no obvious pattern between the long-lived radium isotopes and salinity (Figures S3c and S3d). On the western shelf, the daily average dry deposition of dust particles was 0.05 g m^{-2} d^{-1} (Hsu et al., 2013). Based on Moore (1996), 1 g suspended solids can desorb 2 dpm radium in seawater. Thus, the atmospheric deposition would contribute about

3.4×10^8 dpm day^{-1} radium in the upwelling-influenced area and 6×10^9 dpm day^{-1} in the no-upwelling area, which accounted for no more than 0.3% in the upwelling-influenced area and no more than 1.2% in the no-upwelling area in the radium inventory. The contributions from atmospheric deposition were so small that we ignored this source in the box model.

The higher radium activities (except for ^{228}Ra) in the bottom water relative to the surface water at offshore Stations K3 and K4 (Figures 4i and 4j) implied a radium source from the bottom such as sediment diffusion and SGD. The ^{228}Ra/^{226}Ra ratio in the bottom water was about 1 at these two stations, which is similar to what was reported to be released from the Mississippi shelf sediments, 1.64 (Krest et al., 1999). In our study region, the average ratio of the coastal groundwater was 7.68 ± 2.24. The average ^{228}Ra/^{226}Ra ratio in the Pearl River estuary was 3.01 ± 0.61 (at stations where salinity >0). As discussed in Section 3.2, Transect H was dominated by the Pearl River plume. The ^{228}Ra/^{226}Ra ratios in the surface water at offshore stations (Stations H2–4) fell in the range of 3.11–3.22 due to the Pearl River plume and possibly coastal SGD.

Based on the discussion above, the radium sources in the upwelling-influenced area included the riverine inputs, sediment diffusion, upwelling, SGD, horizontal transport, and atmospheric deposition. In the no-upwelling area, the radium sources were the Pearl River, local rivers, sediment diffusion, SGD, horizontal transport, and atmospheric deposition.

As discussed in Section 2.4.2, Equation 3 can be rewritten as Equation 9 in the upwelling-influenced area and as Equation 10 in the no-upwelling area:

$$\frac{{}^{i}I_1}{t_1} = Q_{quan} \times {}^{i}Ra_{quan} + Q_{wen} \times {}^{i}Ra_{wen} + A_{sed1} \times {}^{i}F_{sed} + Q_{SGD1} \times {}^{i}Ra_{SGD} + v \times A_{uw} \times {}^{i}Ra_{uw} + \Sigma\left(Q_{ht1} \times {}^{i}Ra_{ht1}\right) \tag{9}$$

$$\frac{{}^{i}I_1}{t_2} = Q_{PR} \times {}^{i}Ra_{PR} + Q_{jian} \times {}^{i}Ra_{jian} + Q_{my} \times {}^{i}Ra_{my} + A_{sed2} \times {}^{i}F_{sed} + Q_{SGD2} \times {}^{i}Ra_{SGD} + \Sigma\left(Q_{ht2} \times {}^{i}Ra_{ht2}\right) \tag{10}$$

The parameters used in these equations are listed in Table 1. The upper mixed layer was chosen as the box. The average depth of the mixed layer was 8.0 m in the upwelling-influenced area and 8.8 m in the no-upwelling area. The radium activity at 15 m depth at nearshore Station C1 was used as the upwelling end-member. The upwelling rate was 0.13 m day^{-1} in this area. On the shelf, the riverine contribution is actually what is exported from the estuary. The radium activity at Station F414, taken as the radium exported from the Pearl River estuary, was thus the Pearl River end-member in this study. The river discharge of the Pearl River was the average from the week prior to the sampling to the end of the sampling, 1.2×10^9 m^3 day^{-1}. The radium from sediments was due to molecular diffusion, bioirrigation, and bioturbation. Luo et al. (2018) estimated that the ^{228}Ra fluxes from sediments was 6.3 dpm m^{-2} day^{-1} using the model developed by Nozaki et al. (1990). The global average regeneration rate of ^{226}Ra in sediments is 0.45 dpm m^{-2} day^{-1} (Q. Liu et al., 2012). Following Section 2.4.2, the radium inventory was 1.79×10^{12} dpm for ^{226}Ra and 4.32×10^{12} dpm for ^{228}Ra in the upwelling-influenced area and 1.43×10^{13} dpm for ^{226}Ra and 6.57×10^{13} dpm for ^{228}Ra in the no-upwelling area.

The flux of SGD (in m^3 day^{-1}) based on the ^{226}Ra box model was (0.47–3.0) $\times 10^8$ with an average of (1.5 ± 0.8) $\times 10^8$ in the upwelling-influenced area and (2.0–13) $\times 10^8$ with an average of (6.2 ± 3.3) $\times 10^8$ in the no-upwelling area. The flux based on the ^{228}Ra box model was (1.1–13) $\times 10^7$ with an average of (5.5 ± 3.7) $\times 10^7$ in the upwelling-influenced area and (0.93–11) $\times 10^8$ with an average of (4.7 ± 3.2) $\times 10^8$ in the no-upwelling area.

Figure 5 shows each radium source and its fraction in the total inventory. The radium flux from each source was shown in Table 3. In the upwelling-influenced area, SGD was the greatest ^{226}Ra and ^{228}Ra source, followed by upwelling. In the no-upwelling-influenced area, SGD and the Pearl River contributed the most to the ^{226}Ra and ^{228}Ra inventories. Local rivers, Jianjiang and Moyangjiang Rivers, contributed little to both

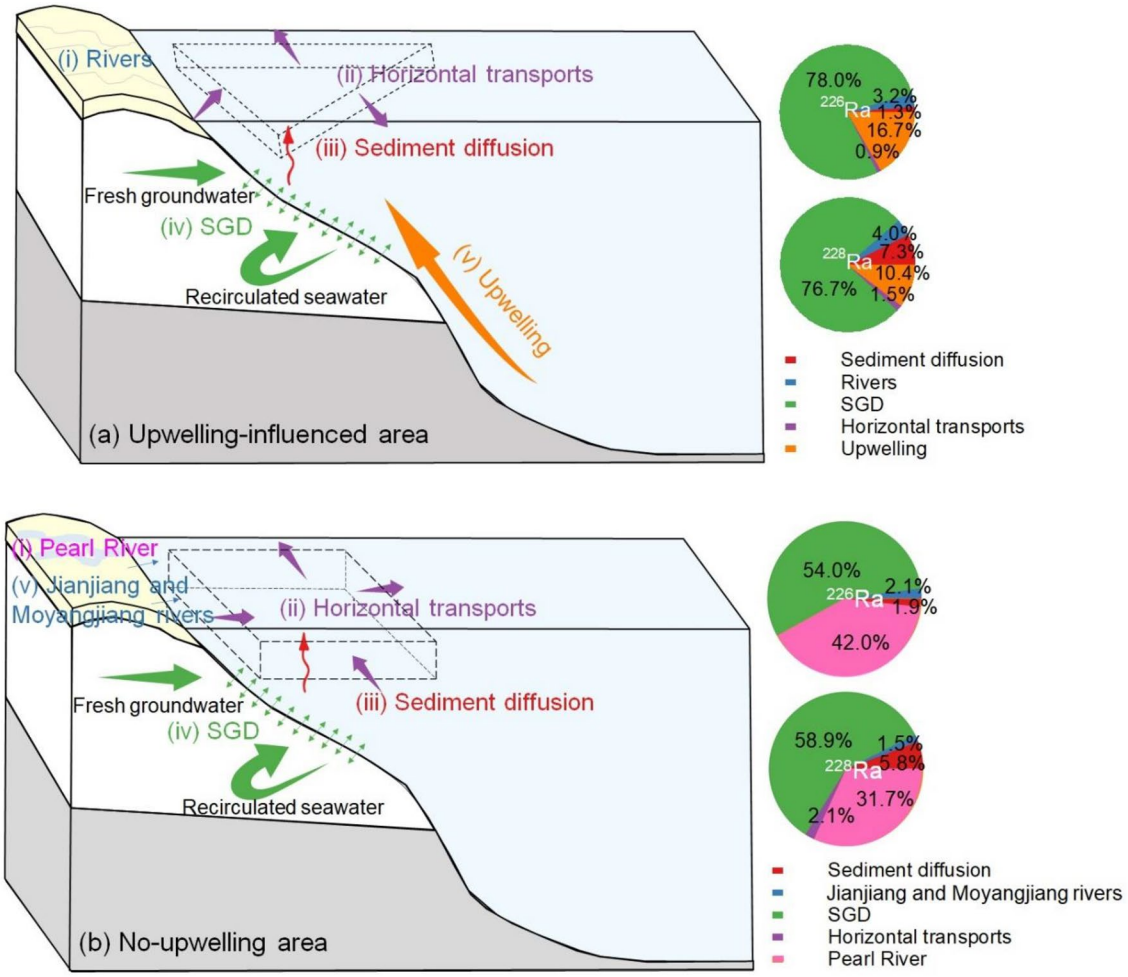

Figure 5. Schematic of the box model based on the long-lived radium isotopes in the upwelling-influenced area and the no-upwelling area on the western shelf of the northern South China Sea from July 28 to August 21, 2012. In the upwelling-influenced area the radium sources include (i) rivers, (ii) horizontal transports, (iii) sediment diffusion, (iv) SGD, and (v) upwelling; and in the no-upwelling area the radium sources include (i) the Pearl River, (ii) horizontal transports, (iii) sediment diffusion, (iv) SGD, and (v) Jianjiang and Moyangjiang Rivers. The pie charts on the right show the proportion of each radium source in the total inventory. SGD, submarine groundwater discharge.

^{226}Ra and ^{228}Ra inventories. Horizontal transports were a loss term for ^{226}Ra in the no-upwelling-influenced area, so it was not shown in the pie chart of ^{226}Ra.

The flux of upwelling and the Pearl River was 4.4×10^8 and 1.2×10^9 m^3 day^{-1}, respectively. The average flux of SGD in the no-upwelling area was up to 6.4×10^8 m^3 day^{-1}, smaller than that of the Pearl River, yet greater than that of upwelling.

The uncertainty in the flux of SGD derived from the box model shown in Figure 6 resulted from the spatial variation in the coastal groundwater end-members in the study area. The error transferred from the measurement error of radium and the spatial variation in the residence time was equivalent to 44% and 35% of the uncertainty resulting from the spatial variation in the coastal groundwater in the upwelling-influenced area and no-upwelling area, respectively (Figure S4).

In the box model, the parameters, such as the Pearl River discharge, the upwelling rate, and the radium activities of the Pearl River end-member and upwelling, were assumed to be constant during the investigation period. However, these parameters might have changed during the investigation. Thus, we evaluated the uncertainty that might be introduced by these assumptions to the overall uncertainty in the flux estimates. According to the results of the box model, sediment diffusion, riverine inputs, and horizontal transports

Table 3
Radium Inputs From Rivers, Horizontal Transports, Sediment Diffusion, SGD, and Upwelling in the Upwelling-Influenced Area and From the Pearl River, Horizontal Transports, Sediment Diffusion, SGD, and Jianjiang and Moyangjiang Rivers in the No-Upwelling Area

			Radium input		
		Radium source	dpm day^{-1}	dpm m^{-1} day^{-1}	dpm m^{-2} day^{-1}
Upwelling-influenced area	^{226}Ra	Rivers	3.79×10^{9}	1.74×10^{4}	1.13
		Horizontal transports	1.11×10^{9}	5.09×10^{3}	0.33
		Sediment diffusion	1.51×10^{9}	6.90×10^{3}	0.45
		SGD	9.29×10^{10}	4.25×10^{5}	27.7
		Upwelling	1.98×10^{10}	9.08×10^{4}	5.93
	^{228}Ra	Rivers	1.17×10^{10}	5.34×10^{4}	3.48
		Horizontal transports	4.22×10^{9}	1.93×10^{4}	1.26
		Sediment diffusion	2.11×10^{10}	9.66×10^{4}	6.30
		SGD	2.21×10^{11}	1.01×10^{6}	66.0
		Upwelling	3.00×10^{10}	1.37×10^{5}	8.97
No-upwelling area	^{226}Ra	Pearl River	3.01×10^{11}	5.66×10^{5}	10.1
		Horizontal transports	-1.04×10^{10}	-1.96×10^{4}	−0.35
		Sediment diffusion	1.35×10^{10}	2.53×10^{4}	0.45
		SGD	3.87×10^{11}	7.27×10^{5}	13.0
		Jianjiang and Moyangjiang Rivers	1.49×10^{10}	2.80×10^{4}	0.50
	^{228}Ra	Pearl River	1.03×10^{12}	1.93×10^{6}	34.3
		Horizontal transports	6.66×10^{10}	1.25×10^{5}	2.23
		Sediment diffusion	1.88×10^{11}	3.58×10^{6}	6.30
		SGD	1.91×10^{12}	3.58×10^{6}	63.7
		Jianjiang and Moyangjiang Rivers	4.97×10^{10}	9.32×10^{4}	1.66

Note. The negative value represents the radium sink.

accounted for no more than 13% in the upwelling-influenced area and 8.4% in the no-upwelling area to the total radium inventory. The upwelling rate was 0.14 ± 1.66 m day^{-1} during the sampling period. With such a variation in the upwelling rate, the SGD flux would vary by 93%–192%. If the radium activity of the upwelling would change by 50%, the SGD flux would change by 3%–28%. The Pearl River discharge was $(1.2 \pm 0.3) \times 10^{9}$ m^{3} day^{-1} during the sampling period. With such a variation in the Pearl River discharge, the SGD flux would vary by 7%–14% in the no-upwelling area. Assume that the radium activity of the Pearl River end-member would vary by 50%, then the flux of SGD would change by 27%–39%.

Please note that our SGD flux based on Ra box models is an estimate for the upper mixed layer depth as in most other SGD studies on the shelf due to the limitation of large sampling demand of radium and the ease of setting up the box model (Q. Liu et al., 2012; Luo et al., 2018; Tan et al., 2018). However, it is likely that SGD may flow through the continental margins below the mixed layer. Therefore, the flux of SGD occurring throughout the whole water column on the shelf may be greater than our estimates.

4.3. The Flux of SGD Calculated With a Three End-Member Mixing Model

In the no-upwelling area, the offshore seawater, the Pearl River, and SGD seemed to be the major end-members for the surface seawater based on the activities of ^{226}Ra and ^{228}Ra since most of the observed data fell in the triangle formed by the three end-members (Figure 7a). Thus, we used the long-lived radium isotopes to establish a three end-member mixing model to estimate the flux of SGD in the no-upwelling area. The end-member values are shown in Table 4. Based on Equations 5–7, the proportion of groundwater ranged from 0.2% to 5.9% in this area (Figure 7b), with an average of 1.9 ± 1.4%. The volume of the no-upwelling

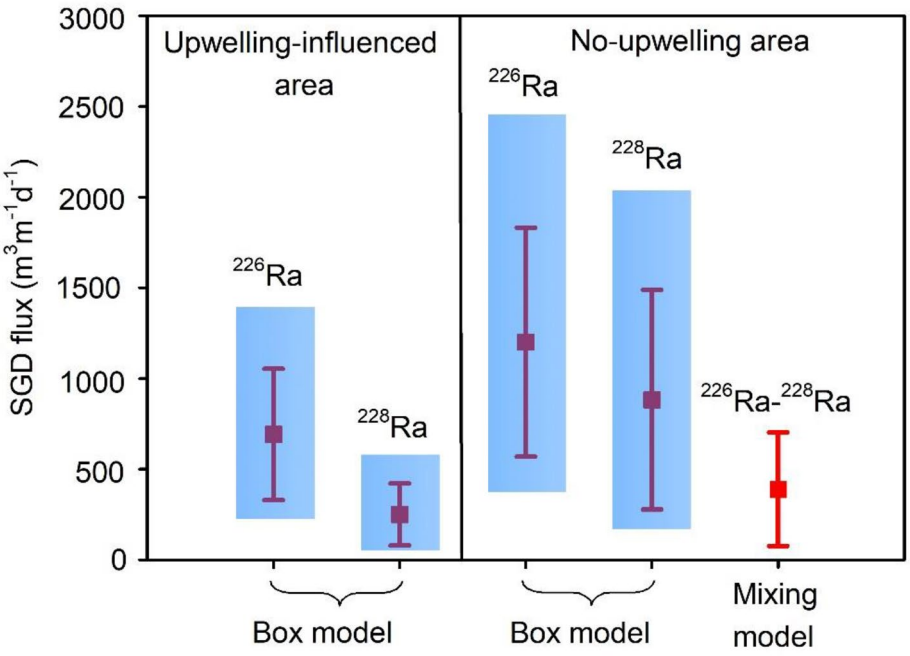

Figure 6. The SGD flux estimated using the three end-member mixing model and the box model in the upwelling-influenced area and the no-upwelling area. The red squares and lines represent the average SGD flux and the uncertainty of the SGD flux, respectively. The blue rectangle shows the range of the SGD flux. SGD, submarine groundwater discharge.

area was about 2.3×10^{11} m^3. Thus, the flux of SGD in the no-upwelling area was estimated to be $(2.1 \pm 1.7) \times 10^8$ m^3 day^{-1}, in the same order of the magnitude as the flux from the box model. The value of the SGD flux derived from the box model, however, was 2–3 times greater than that from the mixing model (Figure 6) because in the three end-member mixing model only the surface water (about 5 m below the surface or even shallower) was involved, while in the box model a deeper layer (8.8 m) was included.

The uncertainty in the flux of SGD based on the mixing model resulted from the uncertainty in the residence time, 40%, and in the spatial variation in the coastal groundwater, 92%. The flux of SGD would change by 8%–25% if the activity of ^{226}Ra or ^{228}Ra in the groundwater would change by 10%.

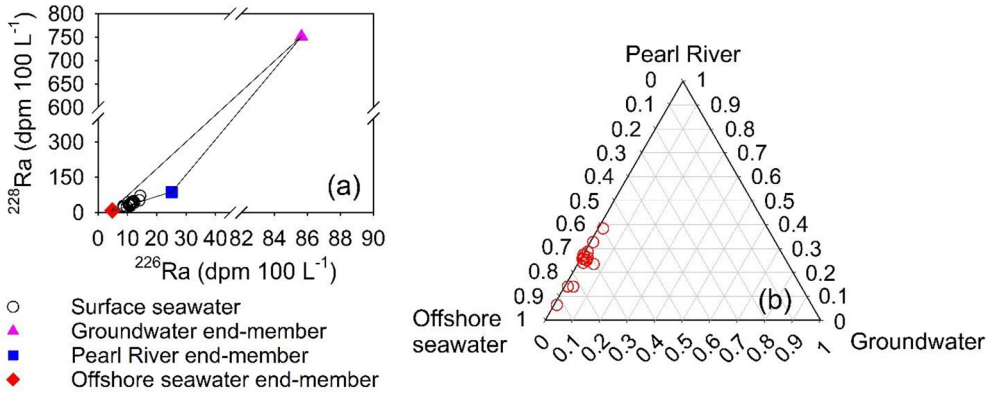

Figure 7. The activity of ^{226}Ra and ^{228}Ra in the surface water in the no-upwelling area and the fractions of groundwater, the Pearl River, and the offshore seawater end-members estimated using a three end-member mixing model with ^{226}Ra and ^{228}Ra as the conservative parameters. (a) ^{226}Ra versus ^{228}Ra, and (b) the fraction of each end-member.

Table 4
The Activities of ^{226}Ra and ^{228}Ra and Salinity of the Three End-Members in the Mixing Model to Estimate the Flux of SGD in the No-Upwelling Area on the Western Shelf of the Northern South China Sea

End-member	^{226}Ra (dpm 100 L^{-1})	^{228}Ra (dpm 100 L^{-1})	Salinity
Pearl River	25 ± 1	86 ± 3	26.4
Offshore seawater	4.9 ± 0.1	8.2 ± 0.3	33.6
Groundwater	86 ± 52	751 ± 643	25.7

For comparison, we normalized our flux of SGD based on the ^{226}Ra box model to shoreline and compiled other shelf-scale fluxes of SGD (Table 5). The coastline was about 218 km long in the upwelling-influenced area and 533 km long in the no-upwelling area. Thus, our SGD rate in the upwelling-influenced area was 215–1382 m^3 m^{-1} day^{-1} with an average of 679 ± 357 m^3 m^{-1} day^{-1}, which is greater than the rate in the summer of 2014 estimated by Luo et al. (2018). The reason for greater rates in our study may be as follows. The study area in Luo et al. (2018) was further offshore and the activity of radium in their study ranged from 5.9 to 13.7 dpm 100 L^{-1} for ^{226}Ra and 6.1–15 dpm 100 L^{-1} for ^{228}Ra, with the outermost station about 115 km offshore, while in our study the activity of the long-lived radium isotopes was greater, 8–11.1 dpm 100 L^{-1} for ^{226}Ra and 15.2–25.5 dpm 100 L^{-1} for ^{228}Ra, with the outermost station located 51 km offshore. In the no-upwelling area, the SGD rate was 368–2364 m^3 m^{-1} day^{-1} with an average of 1161 ± 610 m^3 m^{-1} day^{-1}, which is smaller than the rates of 1,600–4,100 m^3 m^{-1} day^{-1} in the winter of 2010 (Tan et al., 2018). The greater rates in Tan et al. (2018) are due to the fact that the mixed layer was 56 m in the winter of 2010, much greater than 8.8 m in the summer of 2012, resulting in a greater radium inventory and SGD flux. In general, the shoreline normalized flux of SGD on shelf scale varied from a few dozens of m^3 m^{-1} day^{-1} to a few thousands of m^3 m^{-1} day^{-1} (Table 5) and our results were consistent with those on other shelves. For ease of comparing with the SGD rate on embayment scale or estuary scale, our SGD rate was normalized to area, which was 1.4–9.0 cm day^{-1} in the upwelling-influenced area and 0.7–4.2 cm day^{-1} in the no-upwelling area.

4.4. Fluxes of Nutrients, DIC, TA, and DOC Carried by SGD, Upwelling, and the Pearl River

SGD consists of fresh groundwater and recirculated seawater (Burnett et al., 2003). The annual average fresh groundwater recharge rates (Q_{fre}) along the east coast of Hainan Island and western shelf off the Pearl River estuary were 3.5 × 10^6 m^3 day^{-1} (Luo et al., 2018) and 4.1 × 10^7 m^3 day^{-1} (Zhang & Li, 2005), equivalent to 2.3% and 6.4% of the flux of SGD in the upwelling-influenced and no-upwelling areas, respectively. Thus, most of the SGD was recirculated seawater. When calculating the net fluxes of nutrients, DIC, TA, and DOC carried by SGD into the coastal ocean, the contribution of intruding seawater in the subterranean estuary should be deducted with the following equation:

$$F = Q_{SGD} \times C_{SGD} - \left(Q_{SGD} - Q_{fre}\right) \times C_{re} \quad (11)$$

Table 5
The Flux of SGD on Large Scales in Different Regions

Region	Date	Flux of SGD (m^3 m^{-1} day^{-1})	Reference
Mediterranean Sea	1981–2014	12.8–205.5	Rodellas et al. (2015)
Atlantic Ocean	1981–1999	630–1,288	Moore and de Oliveira (2008)
Bohai Sea, China	November 2014	333 ± 216	J. Liu et al. (2017)
South Atlantic Bight, USA	July 1996	70	Moore (1996)
East China Sea	December 2009	2,400–7,200	Tan et al. (2018)
East coast of Hainan Island	August–September 2014	368 ± 98	Luo et al. (2018)
Western shelf off the Pearl River estuary	January 2010	1,600–4,100	Tan et al. (2018)
Eastern shelf off the Pearl River estuary	January 2010	600–1,000	Tan et al. (2018)
Eastern shelf off the Pearl River estuary	June–July 2008	1,104–1,201	Q. Liu et al. (2012)
Southeast coast of Hainan Island	August 2012	215–1,382	This study
Western shelf off the Pearl River estuary	August 2012	368–2,364	This study

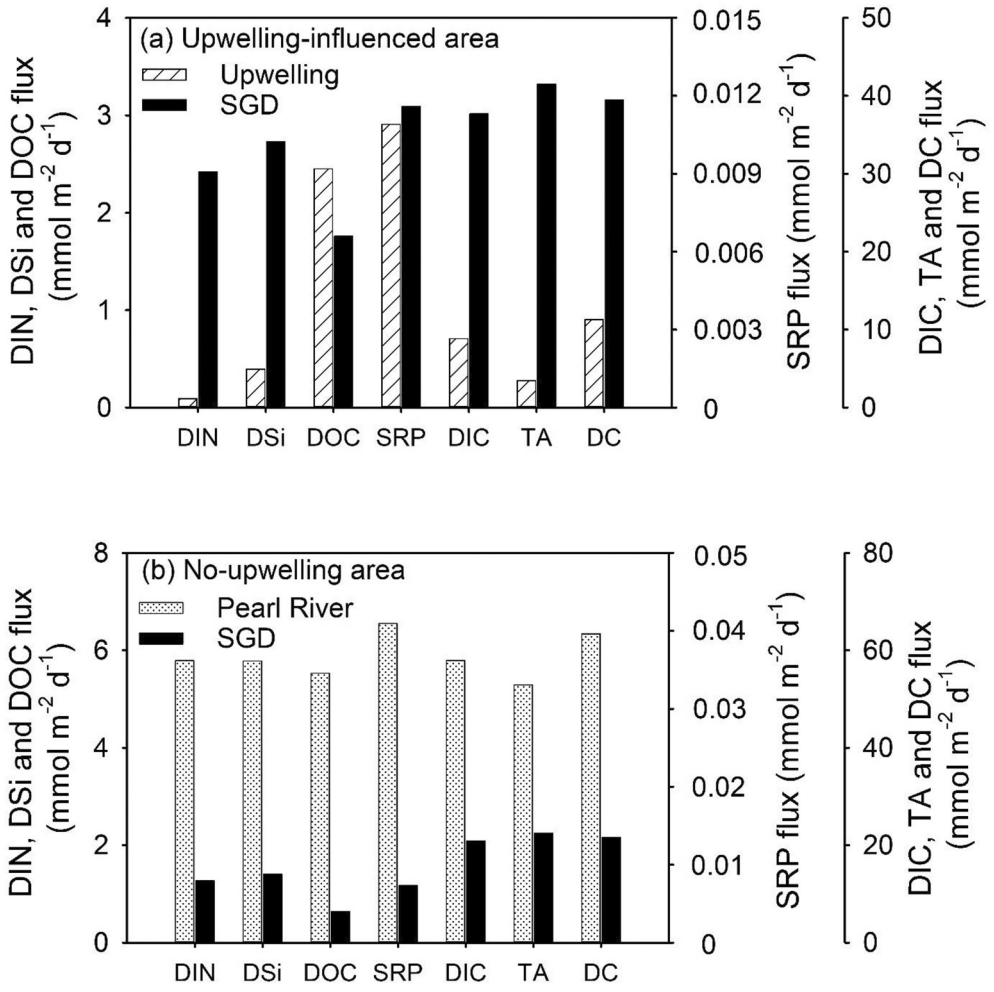

Figure 8. The fluxes of nutrients, DIC, TA, DOC, and DC (a) via the upwelling and SGD in the upwelling-influenced area, and (b) via the Pearl River and SGD in the no-upwelling area. DC, dissolved carbon; DIC, dissolved inorganic carbon; DOC, dissolved organic carbon; SGD, submarine groundwater discharge; TA, total alkalinity.

where F is the net material flux and C_{GW} and C_{re} denote the average material concentration in the coastal groundwater and the recirculated seawater, respectively. The material concentration in the coastal saline groundwater was listed in Table 2. The average material concentration in the bottom water was used as C_{re}. The flux of SGD was the area-normalized flux based on the ^{226}Ra box model, $(4.4 \pm 2.3) \times 10^{-2}$ m^3 m^{-2} day^{-1} in the upwelling-influenced area and $(2.1 \pm 1.1) \times 10^{-2}$ m^3 m^{-2} day^{-1} in the no-upwelling area. Due to nutrients, DIC, TA, and DOC data not available in the coastal groundwater along the east coast of Hainan Island, the concentrations of nutrients, DIC, TA, and DOC in the coastal groundwater in the spring of 2012 sampled along the coast from Zhuhai City to Zhanjiang City were taken as C_{GW} in both the upwelling-influenced area and the no-upwelling area.

Consequently, in the upwelling-influenced area, the material fluxes (in mol m^{-2} day^{-1}) via SGD were 2.42 ± 3.86 for DIN, $(1.16 \pm 2.65) \times 10^{-2}$ for SRP, 2.73 ± 2.42 for DSi, 37.7 ± 46.5 for DIC, 41.5 ± 50.2 for TA, and 1.78 ± 1.89 for DOC. The fluxes of DIN, DSi, DIC, and TA via SGD were 27, 7, 4, and 12 times greater than those from the upwelling, respectively (Figure 8a). The DOC flux via SGD, however, was equivalent to 86% of that from the upwelling. The dissolved carbon (DC), which was the sum of DIC and DOC, via SGD was 4 times greater than that from the upwelling. The flux of SRP via SGD and the upwelling were similar.

In the no-upwelling area, the material fluxes (mol m^{-2} day^{-1}) via SGD were 1.27 ± 1.86 for DIN, $(1.47 \pm 1.40) \times 10^{-2}$ for SRP, 1.40 ± 1.18 for DSi, 20.9 ± 22.4 for DIC, 22.4 ± 24.1 for TA, and $(6.40 \pm 8.44) \times 10^{-1}$ for DOC.

The nutrient flux via SGD was about a quarter equivalent to the Pearl River estuarine exports, 22% for DIN, 18% for SRP, and 24% for DSi. The fluxes of DIC, TA, DOC, and DC via SGD were equivalent to 36%, 42%, 12%, and 34% of the Pearl River estuarine exports, respectively (Figure 8b).

The uncertainty in the material fluxes resulted from the uncertainty in the flux of SGD and the spatial variation in the concentrations of chemicals in the coastal groundwater and recirculated seawater. In the upwelling-influenced area, the spatial variation in the solute concentrations of chemicals was the major source of uncertainty, equivalent to 94%, 91%, 81%, 92%, 91%, and 87% of the total uncertainties in fluxes of DIN, SRP, DSi, DIC, TA, and DOC, respectively, followed by the uncertainty resulting from the flux of SGD, 22%–59% (Table S1). Similarly, in the no-upwelling area, the uncertainty resulting from the spatial variation in the concentrations in the coastal groundwater was equivalent to 93%, 82%, 79%, 90%, 91%, and 93% of the total uncertainties in the fluxes of DIN, SRP, DSi, DIC, TA, and DOC, respectively.

4.5. Primary Production Supported by SGD

According to the N:P ratio (69 ± 97) in the groundwater in this study, the SRP carried by SGD on the shelf would be used up first. The primary production that the SGD-associated SRP can support was 0.10 ± 0.24 mmol C m^{-3} day^{-1} in the upwelling-influence area and 0.21 ± 0.20 mmol C m^{-3} day^{-1} in the no-upwelling area. Luo et al. (2018) suggested that the new production on the eastern Hainan shelf was 0.89 mmol C m^{-3} day^{-1}. The new production on the shelf of the NSCS was 1.68 mmol C m^{-3} day^{-1} (L. Wang, 2011). Thus, the production supported by the SGD-borne SRP contributed 11% and 13% to the new production in the upwelling-influenced area and no-upwelling area, respectively. The DIC and DIN consumed in the production supported by the SGD-borne SRP only accounted for 3% of the DIC and 7% of the DIN carried by SGD in the upwelling-influenced area and 7% and 18% in the no-upwelling area. Most DIN and DIC carried by SGD entered the coastal ocean as net sources of DIN and DIC. With the net flux of DIC via SGD, the concentration of DIC could increase by 46.4 ± 62.4 μmol L^{-1} in the upwelling-influenced area and 51.9 ± 62.3 μmol L^{-1} in the no-upwelling area. With the net input via SGD, the concentration of DIN could increase by 2.84 ± 5.06 μmol L^{-1} in the upwelling-influenced area and 2.78 ± 5.06 μmol L^{-1} in the no-upwelling area. The fluxes of carbon across interfaces on shelf scale, such as the air–sea interface and the river–sea interface, have been well estimated, yet, the flux of carbon associated with SGD was poorly constrained (Q. Liu et al., 2018). Our study reveals that SGD was an important carbon and nutrients source in the shelf budget. Our results provide a necessary supplement to the data base of the fluxes of carbon and nutrients across the land–ocean interface.

4.6. Impacts of SGD in Upwelling-Influenced Areas and River-Dominated Areas

On the western shelf of the NSCS, the SGD flux (in m^3 m^{-1} day^{-1}) in the no-upwelling area was about twice as great as that in the upwelling-influenced area. As for the SGD-derived chemical fluxes (in mmol m^{-1} day^{-1}) in the two areas, the flux of SRP in the no-upwelling area was nearly 5 times as much as that in the upwelling-influenced area. The fluxes of DIN, DSi, DIC, TA, and DC were twice as much. The flux of DOC in the no-upwelling area was 33% greater than that in the upwelling-influenced area. The impacts of SGD in an upwelling-influenced system and a river-dominated system might thus vary due to different material fluxes via SGD and various biogeochemical features in these two systems.

In our upwelling-influenced area, the N:P ratio in the whole water column ranged from 3.1 to 15.6, which were lower than or nearly equal to the Redfield ratio, indicating that the phytoplankton was limited by nitrogen. The nitrogen needed to support the current observed new production in the mixed layer has been shown to be much greater than the known nitrogen loadings (I. I. Lin et al., 2003; McGillicuddy et al., 2007). Based on our results, SGD was a nitrogen source more important than the upwelling in this area. With a high N:P ratio of 69, SGD might significantly promote the production in areas limited by nitrogen in the NSCS.

Coastal upwelling has been demonstrated to be a significant nutrient source and largely increases the primary production (Messié & Chavez, 2015). About 5% of the global ocean primary production has been supported in the eastern boundary current systems, which are no more than 1% of the global ocean and where

coastal upwelling usually occurs (Messié & Chavez, 2015). However, SGD studies in upwelling areas are quite rare. Our study indicates that SGD can be a vital nutrient and carbon source more important than the upwelling in these systems and deserves much more attentions. Because of great spatial differences in aquifer type and hydrodynamic environments, however, we cannot simply extrapolate the SGD contribution in our upwelling-influenced area to other upwelling systems and assess the contribution of SGD to their primary production and nutrient structure.

In the Pearl River-dominated area, phytoplankton and bacterial growths were limited by phosphorus due to the contribution of excess nitrogen from the Pearl River in late summer (Xu et al., 2008), as confirmed by the N:P ratio in our Pearl River end-member (Station F414) of 44. The N:P ratio in the coastal groundwater was 69 ± 97, so that SGD would exacerbate P-limitation in such a P-limited environment. The nutrient flux carried by SGD might have a significant impact on the nutrient structure and phytoplankton compositions and potentially lead to eutrophication and hypoxia off the Pearl River estuary (J. Liu et al., 2018; Richardson, 1997; G. Wang et al., 2018). On the East China Sea shelf, another river-dominated shelf, SGD has been proved to be a major nutrient source (J. Liu et al., 2018; X. Wang et al., 2018). The SGD with a high N:P ratio promoted the *skeletonema* spp., the dominant phytoplankton, during red tides (J. Liu et al., 2018). In addition, Guo et al. (2020) found that SGD was a significant contributor to summer hypoxia in the Changjiang River estuary. We may thus infer that on a river-dominated shelf SGD is usually an important nutrient and carbon source and probably a contributor to eutrophication and hypoxia.

To summarize, the impacts of SGD might vary in an upwelling-influenced system and a river-dominated system considering the differences in the material fluxes via SGD and the nutrient structure in the two systems. In an upwelling-influenced system, which was usually N-limited, SGD with a high N:P ratio would promote the primary production. In contrast, in a river-dominated system, which was usually P-limited due to the riverine inputs, SGD with a high N:P ratio might contribute to coastal eutrophication and subsequent hypoxia.

5. Conclusions

In this study, the flux of SGD was estimated to be (0.11–3.0) × 10^8 m^3 day^{-1} with an average of (1.0 ± 0.43) × 10^8 m^3 day^{-1} along the east coast of Hainan Island, an upwelling-influenced area, based on Ra box models. On the western shelf off the Pearl River estuary, a no-upwelling area, the flux of SGD was estimated to be (0.93–13) × 10^8 m^3 day^{-1} with an average of (5.4 ± 2.3) × 10^8 m^3 day^{-1} based on Ra box models and (2.1 ± 1.7) × 10^8 m^3 day^{-1} based on a three end-member mixing model. The shoreline normalized SGD fluxes were 214–1,382 m^3 m^{-1} day^{-1} for the upwelling-influenced area and 367–2,364 m^3 m^{-1} day^{-1} for the no-upwelling area. The area-normalized SGD rates were 3.0 ± 1.3 and 1.8 ± 0.8 cm day^{-1} in these two areas, respectively.

In the upwelling-influenced area, the net fluxes of DIN, SRP, DSi, DIC, and TA (in mol m^{-2} day^{-1}) carried by SGD were 2.42 ± 3.86, (1.16 ± 2.65) × 10^{-2}, 2.73 ± 2.43, 37.7 ± 46.5, and 41.5 ± 50.2, respectively. The fluxes of DIN, DSi, DIC, and TA via SGD were 27, 7, 4, and 12 times greater than those from the upwelling. The flux of SRP via SGD was similar to that from the upwelling. As for DOC, the flux was 1.76 ± 1.89 mol m^{-2} day^{-1}, which were equivalent to 72% of that carried by the upwelling. The flux of DC was 39.5 ± 68.5 mol m^{-2} day^{-1}, 4 times greater than that from the upwelling. These results indicate that SGD is a N, Si and carbon source more important than the upwelling.

In the no-upwelling area, the net fluxes via SGD (in mol m^{-2} day^{-1}) were 1.27 ± 1.86 for DIN, (1.47 ± 1.40) × 10^{-2} for SRP, 1.40 ± 1.18 for DSi, 20.9 ± 22.4 for DIC, 22.4 ± 24.1 for TA, and (6.40 ± 8.44) × 10^{-1} for DOC. The average net chemical fluxes via SGD were equivalent to 22% for DIN, 18% for SRP, 24% for DSi, 36% for DIC, 42% for TA, and 12% for DOC of those exported from the Pearl River estuary. The average DC flux was 21.6 ± 32.9 mol m^{-2} day^{-1}, equivalent to 34% of that exported from the Pearl River. These results indicate that SGD is an important nutrient and carbon source second to the Pearl River on the western shelf off the Pearl River estuary in the summer of 2012.

The SRP carried by SGD could support primary production of 0.10 ± 0.24 mmol C m^{-3} day^{-1} in the upwelling-influenced area, accounting for 11% of the new production, and 0.21 ± 0.20 mmol C m^{-3} day^{-1} in

the no-upwelling area, accounting for around 13% of the new production. The concentration of DIC would increase by 46.4 ± 62.4 μmol L^{-1} in the upwelling-influenced area and 51.9 ± 62.3 μmol L^{-1} in the no-upwelling area due to the net flux of DIC via SGD, suggesting that SGD is an important carbon source in the shelf carbon budget.

The flux of SGD and the net material fluxes via SGD were greater in the no-upwelling area than in the upwelling area. Due to different nutrient structures in these two areas, the biogeochemical impacts of SGD might vary.

Data Availability Statement

The data for this research are provided in Table S2 in the supporting information and will be updated with DOI when it is assigned by Pangaea.

Acknowledgments
The study was funded by the National Basic Research Program of China (no. 2015CB954001), the Hong Kong Research Grants Council under the Theme-based Research Scheme (TRS) through grant T21-602/16-R, and National Natural Science Foundation of China (no. 41576074). We are grateful to the crew on R/V Dongfanghong II for their assistance during the cruise. We appreciate the CTD data from Jia Zhu and Zhenyu Sun. We thank Zhiqiang Liu for providing the model data to estimate the upwelling rate and horizontal transport rates and Shuling Wang for sampling and measurements.

References

Bratton, J. F. (2010). The three scales of submarine groundwater flow and discharge across passive continental margins. *The Journal of Geology*, *118*(5), 565–575. https://doi.org/10.1086/655114

Burnett, W. C., Bokuniewicz, H., Huettel, M., Moore, W. S., & Taniguchi, M. (2003). Groundwater and pore water inputs to the coastal zone. *Biogeochemistry*, *66*(1/2), 3–33.

Callahan, J., Dai, M. H., Chen, R. F., Li, X. L., Lu, Z. M., & Huang, W. (2004). Distribution of dissolved organic matter in the Pearl River estuary, China. *Marine Chemistry*, *89*(1–4), 211–224. https://doi.org/10.1016/j.marchem.2004.02.013

Cao, Z. M., Dai, M. H., Zheng, N., Wang, D. L., Li, Q., Zhai, W. D., et al. (2011). Dynamics of the carbonate system in a large continental shelf system under the influence of both a river plume and coastal upwelling. *Journal of Geophysical Research*, *116*, G02010. https://doi.org/10.1029/2010JG001596

Charette, M. A., Henderson, P. B., Breier, C. F., & Liu, Q. (2013). Submarine groundwater discharge in a river-dominated Florida estuary. *Marine Chemistry*, *156*, 3–17. https://doi.org/10.1016/j.marchem.2013.04.001

Dong, X., Huang, H., Zheng, N., Pan, A., Wang, S., Huo, C., et al. (2017). Acidification mediated by a river plume and coastal upwelling on a fringing reef at the east coast of Hainan Island, northern South China Sea. *Journal of Geophysical Research: Oceans*, *122*, 7521–7536. https://doi.org/10.1002/2017JC013228

Eleftheriou, G., Tsabaris, C., Patiris, D. L., Androulakaki, E. G., & Vlastou, R. (2017). Estimation of coastal residence time of submarine groundwater discharge using radium progenies. *Applied Radiation and Isotopes*, *121*, 44–50. https://doi.org/10.1016/j.apradiso.2016.12.021

Elsinger, R. J., King, P. T., & Moore, W. S. (1982). Radium-224 in natural waters measured by γ-ray spectrometry. *Analytica Chimica Acta*, *144*, 277–281.

Gan, J. P., Cheung, A., Guo, X. G., & Li, L. (2009). Intensified upwelling over a widened shelf in the northeastern South China Sea. *Journal of Geophysical Research*, *114*, C09019. https://doi.org/10.1029/2007JC004660

Gan, J. P., Lu, Z. M., Dai, M. H., Cheung, A. Y. Y., Liu, H. B., & Harrison, P. (2010). Biological response to intensified upwelling and to a river plume in the northeastern South China Sea: A modeling study. *Journal of Geophysical Research*, *115*, C09001. https://doi.org/10.1029/2009JC005569

Gómez-Álvarez, P., Bates, B., Santos, I. R., Escobar Correa, R., Tucker, J. P., Ibrahim, N., et al. (2019). Submarine groundwater discharge revealed by ^{224}Ra and ^{223}Ra in Coffs Harbor, Australia. *Journal of Radioanalytical and Nuclear Chemistry*, *319*(3), 1193–1199. https://doi.org/10.1007/s10967-019-06412-0

Guo, X., Cai, W.-J., Zhai, W., Dai, M., Wang, Y., & Chen, B. (2008). Seasonal variations in the inorganic carbon system in the Pearl River (Zhujiang) estuary. *Continental Shelf Research*, *28*(12), 1424–1434. https://doi.org/10.1016/j.csr.2007.07.011

Guo, X., Xu, B., Burnett, W. C., Wei, Q., Nan, H., Zhao, S., et al. (2020). Does submarine groundwater discharge contribute to summer hypoxia in the Changjiang (Yangtze) River Estuary? *The Science of the Total Environment*, *719*, 137450. https://doi.org/10.1016/j.csr.2007.07.011

Han, A., Dai, M., Kao, S.-J., Gan, J., Li, Q., Wang, L., et al. (2012). Nutrient dynamics and biological consumption in a large continental shelf system under the influence of both a river plume and coastal upwelling. *Limnology & Oceanography*, *57*(2), 486–502.

Hsu, S.-C., Tsai, F., Lin, F.-J., Chen, W.-N., Shiah, F.-K., Huang, J.-C., et al. (2013). A super Asian dust storm over the East and South China Seas: Disproportionate dust deposition. *Journal of Geophysical Research: Atmospheres*, *118*, 7169–7181. https://doi.org/10.1002/jgrd.50405

Hwang, D.-W., Lee, Y.-W., & Kim, G. (2005). Large submarine groundwater discharge and benthic eutrophication in Bangdu Bay on volcanic Jeju Island, Korea. *Limnology & Oceanography*, *50*(5), 1393–1403.

Ji, T., Du, J., Moore, W. S., Zhang, G., Su, N., & Zhang, J. (2013). Nutrient inputs to a Lagoon through submarine groundwater discharge: The case of Laoye Lagoon, Hainan, China. *Journal of Marine Systems*, *111–112*, 253–262. https://doi.org/10.1016/j.jmarsys.2012.11.007

Jing, Z.-Y., Qi, Y.-Q., Hua, Z.-L., & Zhang, H. (2009). Numerical study on the summer upwelling system in the northern continental shelf of the South China Sea. *Continental Shelf Research*, *29*(2), 467–478. https://doi.org/10.1016/j.csr.2008.11.008

Kim, G., Kim, J.-S., & Hwang, D.-W. (2011). Submarine groundwater discharge from oceanic islands standing in oligotrophic oceans: Implications for global biological production and organic carbon fluxes. *Limnology & Oceanography*, *56*(2), 673–682. https://doi.org/10.4319/lo.2011.56.2.0673

Krest, J. M., Moore, W. S., & Rama (1999). ^{226}Ra and ^{228}Ra in the mixing zones of the Mississippi and Atchafalaya Rivers: Indicators of groundwater input. *Marine Chemistry*, *64*(3), 129–152.

Lee, H., Kim, G., Kim, J., Park, G., & Song, K.-H. (2014). Tracing the flow rate and mixing ratio of the Changjiang diluted water in the northwestern Pacific marginal seas using radium isotopes. *Geophysical Research Letters*, *41*, 4637–4645. https://doi.org/10.1002/2014GL060230

Li, M., Xie, L., Zong, X., Zhang, S., Zhou, L., & Li, J. (2018). The cruise observation of turbulent mixing in the upwelling region east of Hainan Island in the summer of 2012. *Acta Oceanologica Sinica*, *37*(9), 1–12. https://doi.org/10.1007/s13131-018-1260-y

Li, Q. (2014). Status evaluation and trend analysis of Jianjiang water quality in Maoming City. *Guangdong Water Resources and Hydropower*, (2), 54–56.

Lin, I. I., Liu, W. T., Wu, C.-C., Wong, G. T. F., & Liu, K.-K. (2003). New evidence for enhanced primary production triggered by tropical cyclone. *Geophysical Research Letters*, *30*(13), 1718. https://doi.org/10.1029/2003GL017141

Lin, P., Cheng, P., Gan, J., & Hu, J. (2016). Dynamics of wind-driven upwelling off the northeastern coast of Hainan Island. *Journal of Geophysical Research: Oceans*, *121*, 1160–1173. https://doi.org/10.1002/2015JC011000

Lin, P., Hu, J., Zheng, Q., Sun, Z., & Zhu, J. (2016). Observation of summertime upwelling off the eastern and northeastern coasts of Hainan Island, China. *Ocean Dynamics*, *66*(3), 387–399. https://doi.org/10.1007/s10236-016-0934-2

Liu, J., Du, J., Wu, Y., & Liu, S. (2018). Nutrient input through submarine groundwater discharge in two major Chinese estuaries: The Pearl River estuary and the Changjiang River estuary. *Estuarine, Coastal and Shelf Science*, *203*, 17–28. https://doi.org/10.1016/j.ecss.2018.02.005

Liu, J., Du, J., & Yi, L. (2017). Ra tracer-based study of submarine groundwater discharge and associated nutrient fluxes into the Bohai Sea, China: A highly human-affected marginal sea. *Journal of Geophysical Research: Oceans*, *122*, 8646–8660. https://doi.org/10.1002/2017JC013095

Liu, L., Li, J., Tan, W., Wu, Y., Liu, Y., & Wang, H. (2018). Extreme sea level rise off the northwest coast of the South China Sea in 2012. *Journal of Ocean University of China*, *17*(5), 991–999. https://doi.org/10.1007/s11802-018-3681-9

Liu, Q., Charette, M. A., Henderson, P. B., McCorkle, D. C., Martin, W., & Dai, M. (2014). Effect of submarine groundwater discharge on the coastal ocean inorganic carbon cycle. *Limnology & Oceanography*, *59*(5), 1529–1554. https://doi.org/10.4319/lo.2014.59.5.1529

Liu, Q., Dai, M., Chen, W., Huh, C.-A., Wang, G., Li, Q., & Charette, M. A. (2012). How significant is submarine groundwater discharge and its associated dissolved inorganic carbon in a river-dominated shelf system? *Biogeosciences*, *9*(5), 1777–1795. https://doi.org/10.5194/bg-9-1777-2012

Liu, Q., Guo, X., Yin, Z., Zhou, K., Roberts, E. G., & Dai, M. (2018). Carbon fluxes in the China Seas: An overview and perspective. *Science China Earth Sciences*, *61*(11), 1564–1582. https://doi.org/10.1007/s11430-017-9267-4

Luo, X., Jiao, J. J., Liu, Y., Zhang, X., Liang, W., & Tang, D. (2018). Evaluation of water residence time, submarine groundwater discharge, and maximum new production supported by groundwater borne nutrients in a coastal upwelling shelf system. *Journal of Geophysical Research: Oceans*, *123*, 631–655. https://doi.org/10.1002/2017JC013398

McCoy, C., Viso, R., Peterson, R. N., Libes, S., Lewis, B., Ledoux, J., et al. (2011). Radon as an indicator of limited cross-shelf mixing of submarine groundwater discharge along an open ocean beach in the South Atlantic Bight during observed hypoxia. *Continental Shelf Research*, *31*(12), 1306–1317. https://doi.org/10.1016/j.csr.2011.05.009

McGillicuddy, D. J., Anderson, L. A., Bates, N. R., Bibby, T., Buesseler, K. O., Carlson, C. A., et al. (2007). Eddy/wind interactions stimulate extraordinary mid-ocean plankton blooms. *Science*, *316*, 1021–1026.

Men, W., Jiang, Y., Liu, G., Wang, F., & Zhang, Y. (2016). Study of water mixing in the coastal waters of the western Taiwan Strait based on radium isotopes. *Journal of Environmental Radioactivity*, *152*, 16–22. https://doi.org/10.1016/j.jenvrad.2015.11.003

Messié, M., & Chavez, F. P. (2015). Seasonal regulation of primary production in eastern boundary upwelling systems. *Progress in Oceanography*, *134*, 1–18. https://doi.org/10.11867/j.issn.1001-8166.2010.01.0033

Michel, J., Moore, W. S., & King, P. T. (1981). γ-Ray spectrometry for determination of radium-228 and radium-226 in natural waters. *Analytical Chemistry*, *53*(12), 1885–1889.

Moore, W. S. (1976). Sampling ^{228}Ra in the deep ocean. *Deep Sea Research and Oceanographic Abstracts*, *23*(7), 647–651.

Moore, W. S. (1996). Large groundwater inputs to coastal waters revealed by ^{226}Ra enrichments. *Nature*, *380*(6575), 612–614.

Moore, W. S. (2000). Ages of continental shelf waters determined from ^{223}Ra and ^{224}Ra. *Journal of Geophysical Research*, *105*(C9), 22117–22122. https://doi.org/10.1029/1999JC000289

Moore, W. S. (2003). Sources and fluxes of submarine groundwater discharge delineated by radium isotopes. *Biogeochemistry*, *66*(1/2), 75–93.

Moore, W. S. (2007). Fifteen years experience in measuring ^{224}Ra and ^{223}Ra by delayed-coincidence counting. *Marine Chemistry*, *109*(3–4), 188–197. https://doi.org/10.1016/j.marchem.2007.06.015

Moore, W. S. (2010). The effect of submarine groundwater discharge on the ocean. *Annual Review of Marine Science*, *2*, 59–88. https://doi.org/10.1146/annurev-marine-120308-081019

Moore, W. S., & Arnold, R. (1996). Measurement of ^{223}Ra and ^{224}Ra in coastal waters using a delayed coincidence counter. *Journal of Geophysical Research*, *101*(C1), 1321–1329. https://doi.org/10.1029/95JC03139

Moore, W. S., Blanton, J. O., & Joye, S. B. (2006). Estimates of flushing times, submarine groundwater discharge, and nutrient fluxes to Okatee Estuary, South Carolina. *Journal of Geophysical Research*, *111*, C09006. https://doi.org/10.1029/2005JC003041

Moore, W. S., & de Oliveira, J. (2008). Determination of residence time and mixing processes of the Ubatuba, Brazil, inner shelf waters using natural Ra isotopes. *Estuarine, Coastal and Shelf Science*, *76*(3), 512–521. https://doi.org/10.1016/j.ecss.2007.07.042

Moore, W. S., & Dymond, J. (1984). Radium isotope measurements using germanium detectors. *Nuclear Instruments and Methods in Physics Research*, *223*(2), 407–411.

Moore, W. S., Sarmiento, J. L., & Key, R. M. (2008). Submarine groundwater discharge revealed by ^{228}Ra distribution in the upper Atlantic Ocean. *Nature Geoscience*, *1*(5), 309–311. https://doi.org/10.1038/ngeo183

Niino, H., & Emery, K. O. (1961). Sediments of shallow portions of East China Sea and South China Sea. *Geological Society of America Bulletin*, *72*(5), 731–762.

Nozaki, Y., Kasemsupaya, V., & Tsubota, H. (1989). Mean residence time of the shelf water in the East China and the Yellow Seas determined by ^{228}Ra/^{226}Ra measurements. *Geophysical Research Letters*, *16*(11), 1297–1300.

Nozaki, Y., Yamada, M., & Nikaido, H. (1990). The marine geochemistry of actinium-227: Evidence for its migration through sediment pore water. *Geophysical Research Letters*, *17*(11), 1933–1936.

Ou, S., Zhang, H., & Wang, D.-x. (2009). Dynamics of the buoyant plume off the Pearl River estuary in summer. *Environmental Fluid Mechanics*, *9*(5), 471–492. https://doi.org/10.1007/s10652-009-9146-3

Pang, H. L., Gao, H. W., Song, P. P., You, D. W., & Chen, J. (2006). Analysis of diffuse route of the Zhujiang River diluted water in Summer. *Marine Forecasts*, *23*(3), 58–63.

Redfield, A. C., Ketchum, B. H., & Richards, F. A. (1963). The influence of organisms on composition of seawater. In M. N. Hill (Ed.), *The sea* (Vol. 2, pp. 26–77). New York: Interscience.

Richardson, K. (1997). Harmful or exceptional phytoplankton blooms in the marine ecosystem. *Advances in Marine Biology*, *31*(8), 301–385.

Rodellas, V., Garcia-Orellana, J., Masqué, P., Feldman, M., & Weinstein, Y. (2015). Submarine groundwater discharge as a major source of nutrients to the Mediterranean Sea. *Proceedings of the National Academy of Sciences of the United States of America*, *112*(13), 3926–3930. https://doi.org/10.1073/pnas.1419049112

Sadat-Noori, M., Maher, D. T., & Santos, I. R. (2015). Groundwater discharge as a source of dissolved carbon and greenhouse gases in a subtropical estuary. *Estuaries and Coasts*, *39*(3), 639–656. https://doi.org/10.1007/s12237-015-0042-4

Santos, I. R., de Weys, J., Tait, D. R., & Eyre, B. D. (2012). The contribution of groundwater discharge to nutrient exports from a coastal catchment: Post-flood seepage increases estuarine N/P ratios. *Estuaries and Coasts*, *36*(1), 56–73. https://doi.org/10.1007/s12237-012-9561-4

Santos, I. R., Glud, R. N., Maher, D., Erler, D., & Eyre, B. D. (2011). Diel coral reef acidification driven by porewater advection in permeable carbonate sands, Heron Island, Great Barrier Reef. *Geophysical Research Letters*, *38*, L03604. https://doi.org/10.1029/2010GL046053

Srinivasamoorthy, K., Ponnumani, G., Prakash, R., Gopinath, S., Saravanan, K., & Vinnarasi, F. (2018). Tracing groundwater inputs to Bay of Bengal from Sankarabarani River Basin, Pondicherry, India, using continuous radon monitoring. *International journal of Environmental Science and Technology*, *16*(10), 5513–5524. https://doi.org/10.1007/s13762-018-1938-x

Su, N., Du, J., Moore, W. S., Liu, S., & Zhang, J. (2011). An examination of groundwater discharge and the associated nutrient fluxes into the estuaries of eastern Hainan Island, China using ^{226}Ra. *The Science of the Total Environment*, *409*(19), 3909–3918. https://doi.org/10.1016/j.scitotenv.2011.06.017

Su, N., Du, J. Z., Ji, T., & Zhang, J. (2011). ^{226}Ra and ^{228}Ra tracer study on nutrient transport in east coastal waters of Hainan Island, China. *Water Science and Engineering*, *4*(2), 157–169.

Takeoka, H. (1984). Fundamental concepts of exchange and transport time scales in a coastal sea. *Continental Shelf Research*, *3*(3), 311–326.

Tan, E., Wang, G., Moore, W. S., Li, Q., & Dai, M. (2018). Shelf-scale submarine groundwater discharge in the northern South China Sea and East China Sea and its geochemical impacts. *Journal of Geophysical Research: Oceans*, *123*, 2997–3013. https://doi.org/10.1029/2017JC013405

Taylor, J. R. (1997). *An introduction to error analysis* (2nd ed., pp. 1–37). Sausalito, California: University Science Books.

Trezzi, G., Garcia-Orellana, J., Rodellas, V., Santos-Echeandia, J., Tovar-Sánchez, A., Garcia-Solsona, E., & Masqué, P. (2016). Submarine groundwater discharge: A significant source of dissolved trace metals to the North Western Mediterranean Sea. *Marine Chemistry*, *186*, 90–100.

Wang, G., Han, A., Chen, L., Tan, E., & Lin, H. (2018). Fluxes of dissolved organic carbon and nutrients via submarine groundwater discharge into subtropical Sansha Bay, China. *Estuarine, Coastal and Shelf Science*, *207*, 269–282.

Wang, G., Jing, W., Wang, S., Xu, Y., Wang, Z., Zhang, Z., et al. (2014). Coastal acidification induced by tidal-driven submarine groundwater discharge in a coastal coral reef system. *Environmental Science & Technology*, *48*(22), 13069–13075. https://doi.org/10.1021/es5026867

Wang, G., Wang, Z., Zhai, W., Moore, W. S., Li, Q., Yan, X., et al. (2015). Net subterranean estuarine export fluxes of dissolved inorganic C, N, P, Si, and total alkalinity into the Jiulong River estuary, China. *Geochimica et Cosmochimica Acta*, *149*, 103–114. https://doi.org/10.1016/j.gca.2014.11.001

Wang, L. (2011). *New production in the East China Sea and northern South China Sea* (Master's thesis). Retrieved from Xiamen University Electronic Thesis and Dissertations. (https://etd.xmu.edu.cn/detail.asp?serial=55B99BA7-8B27-47D0-9386-B12DF9AC7258) Xiamen: Xiamen University.

Wang, X., Baskaran, M., Su, K., & Du, J. (2018). The important role of submarine groundwater discharge (SGD) to derive nutrient fluxes into river dominated ocean margins—The East China Sea. *Marine Chemistry*, *204*, 121–132. https://doi.org/10.1016/j.marchem.2018.05.010

Wang, X., & Du, J. (2016). Submarine groundwater discharge into typical tropical lagoons: A case study in eastern Hainan Island, China. *Geochemistry, Geophysics, Geosystems*, *17*, 4366–4382. https://doi.org/10.1002/2016GC006502

Xu, J., Yin, K. D., He, L., Yuan, X. C., Ho, A. Y. T., & Harrison, P. J. (2008). Phosphorus limitation in the northern South China Sea during late summer: Influence of the Pearl River. *Deep Sea Research Part I: Oceanographic Research Papers*, *55*(10), 1330–1342.

Yin, S., & Torgersen, T. (1998). The effects of water content and Mn-fiber surface conditions on ^{224}Ra measurement by ^{220}Rn emanation. *Marine Chemistry*, *62*(3–4), 299–306.

Zhang, Z. G., & Li, L. R. (2005). *Groundwater resources of China* (in Chinese). Beijing: Sinomap Press.

Zimmerman, J. T. F. (1976). Mixing and flushing of tidal embayments in the western Dutch Wadden Sea part I: Distribution of salinity and calculation of mixing time scales. *Netherlands Journal of Sea Research*, *10*(2), 149–191.